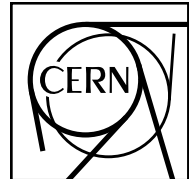


EUROPEAN ORGANISATION FOR NUCLEAR RESEARCH (CERN)



CERN-PH-EP-2014-112

Submitted to: JHEP

Search for direct pair production of the top squark in all-hadronic final states in proton–proton collisions at $\sqrt{s} = 8$ TeV with the ATLAS detector

The ATLAS Collaboration

Abstract

The results of a search for direct pair production of the scalar partner to the top quark using an integrated luminosity of 20.1 fb^{-1} of proton–proton collision data at $\sqrt{s} = 8$ TeV recorded with the ATLAS detector at the LHC are reported. The top squark is assumed to decay via $\tilde{t} \rightarrow t\tilde{\chi}_1^0$ or $\tilde{t} \rightarrow b\tilde{\chi}_1^\pm \rightarrow bW^{(*)}\tilde{\chi}_1^0$, where $\tilde{\chi}_1^0$ ($\tilde{\chi}_1^\pm$) denotes the lightest neutralino (chargino) in supersymmetric models. The search targets a fully-hadronic final state in events with four or more jets and large missing transverse momentum. No significant excess over the Standard Model background prediction is observed, and exclusion limits are reported in terms of the top squark and neutralino masses and as a function of the branching fraction of $\tilde{t} \rightarrow t\tilde{\chi}_1^0$. For a branching fraction of 100%, top squark masses in the range 270–645 GeV are excluded for $\tilde{\chi}_1^0$ masses below 30 GeV. For a branching fraction of 50% to either $\tilde{t} \rightarrow t\tilde{\chi}_1^0$ or $\tilde{t} \rightarrow b\tilde{\chi}_1^\pm$, and assuming the $\tilde{\chi}_1^\pm$ mass to be twice the $\tilde{\chi}_1^0$ mass, top squark masses in the range 250–550 GeV are excluded for $\tilde{\chi}_1^0$ masses below 60 GeV.

1 Introduction

The recent observation of the Standard Model (SM) Higgs boson [1, 2] has brought renewed attention to the gauge hierarchy problem [3–6]. However, the existence (and mass) of this fundamental scalar boson does not resolve the tension between the electroweak and Planck scales. Supersymmetry (SUSY) [7–15] provides an extension of the SM which can resolve the hierarchy problem [16–21] by introducing supersymmetric partners of the known bosons and fermions. The dominant contribution to the divergence of the Higgs boson mass arises from loop diagrams involving the top quark; these can be largely cancelled if a scalar partner of the top quark (top squark) exists and has a mass below ~ 1 TeV [22, 23]. Furthermore, a compelling by-product of R -parity conserving SUSY models [16, 24–27] is a weakly interacting, stable, lightest supersymmetric particle (LSP): a possible candidate for dark matter.

In SUSY models, there are two scalar partners for the top quark (denoted \tilde{t}_L and \tilde{t}_R), corresponding to left-handed and right-handed top quarks. Due to the large Yukawa coupling of the top quark, there can be significant mixing between \tilde{t}_L and \tilde{t}_R , leading to a large splitting between the two mass eigenstates, denoted \tilde{t}_1 and \tilde{t}_2 , where \tilde{t}_1 refers to the lighter of the two states. To leading order the direct top squark production cross section is given in perturbative Quantum Chromodynamics by gluon-gluon and $q\bar{q}$ fusion and depends only on the \tilde{t}_1 mass [28–30]. The decay of the top squark depends on the left-right admixture as well as on the masses and mixing parameters of the fermionic partners of the electroweak and Higgs bosons (collectively known as charginos, $\tilde{\chi}_i^\pm$, $i = 1, 2$ and neutralinos, $\tilde{\chi}_i^0$, $i = 1–4$) to which the top squark can decay. No assumption is made on the LSP mass in this paper. While the LSP is assumed to be the $\tilde{\chi}_1^0$ it could, for example, be a very light gravitino (the fermionic partner of the graviton), which would evade existing limits on the neutralino mass. In addition, \tilde{t}_1 is assumed to be heavier than the top quark and to decay via either $\tilde{t}_1 \rightarrow t\tilde{\chi}_1^0$ or $\tilde{t}_1 \rightarrow b\tilde{\chi}_1^\pm \rightarrow bW^{(*)}\tilde{\chi}_1^0$, as illustrated in figure 1.

This paper presents the results of a search for direct pair production of \tilde{t}_1 using a dataset corresponding to an integrated luminosity of $\int \mathcal{L} dt = 20.1 \text{ fb}^{-1}$. These data were collected by the ATLAS detector at the Large Hadron Collider (LHC) through proton-

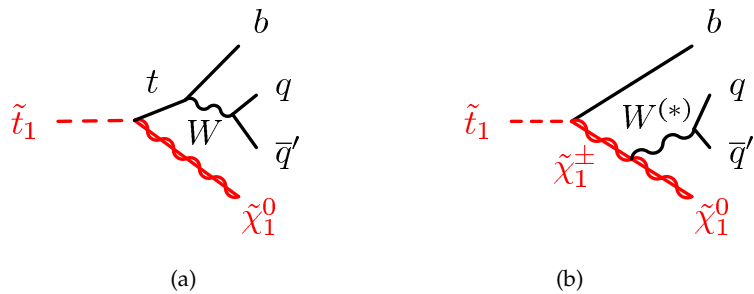


Figure 1. Feynman diagrams illustrating the \tilde{t}_1 decay modes considered: (a) $\tilde{t}_1 \rightarrow t\tilde{\chi}_1^0$ and (b) $\tilde{t}_1 \rightarrow b\tilde{\chi}_1^\pm \rightarrow bW^{(*)}\tilde{\chi}_1^0$.

proton collisions at a centre-of-mass energy of $\sqrt{s} = 8$ TeV. Only fully hadronic final states are considered. The undetected LSP, $\tilde{\chi}_1^0$, leads to missing transverse momentum ($\mathbf{p}_T^{\text{miss}}$, whose magnitude is referred to as E_T^{miss}). If both top squarks decay via $\tilde{t}_1 \rightarrow t\tilde{\chi}_1^0$, the experimental signature is a pair of reconstructed hadronic top quarks plus significant E_T^{miss} . The $b\tilde{\chi}_1^\pm \rightarrow bW^{(*)}\tilde{\chi}_1^0$ decay mode leads to a similar final-state topology, apart from the mass of the resulting hadronic system. The results are presented as a function of the branching fraction $B(\tilde{t}_1 \rightarrow t\tilde{\chi}_1^0)$.

Previous searches for R -parity-conserving direct top squark production at centre-of-mass energies of 7 and 8 TeV have been reported by the ATLAS [31–37] and CMS [38–43] collaborations. The previous ATLAS search in the all-hadronic channel [32] considered only the nominal “fully resolved” experimental signature of six distinct jets (two from the bottom quarks and two from each of the W decays) and significant missing transverse momentum from the LSPs. In this paper, the experimental sensitivity to this signature is enhanced by considering in addition “partially resolved” events with four or five jets in the final state, which can occur if one or more jets are below the reconstruction threshold or if the decay products of Lorentz-boosted top quarks are sufficiently collimated. Furthermore, the sensitivity to the $\tilde{t}_1 \rightarrow b\tilde{\chi}_1^\pm$ decays is augmented by including events with exactly five jets in the final state (targeting final states where one of the jets from the $W^{(*)}$ decay has low transverse momentum, p_T).

2 The ATLAS detector

The ATLAS detector [44] consists of inner tracking devices surrounded by a superconducting solenoid, electromagnetic and hadronic calorimeters and a muon spectrometer in a toroidal magnetic field. The inner detector, in combination with the 2 T field from the solenoid, provides precise tracking of charged particles for $|\eta| < 2.5$.¹ It consists of a silicon pixel detector, a silicon strip detector and a straw-tube tracker that also provides transition radiation measurements for electron identification. A high-granularity electromagnetic calorimeter system, with acceptance covering $|\eta| < 3.2$, uses liquid argon (LAr) as the active medium. A scintillator-tile calorimeter provides hadronic coverage for $|\eta| < 1.7$. The end-cap and forward regions, spanning $1.5 < |\eta| < 4.9$, are instrumented with LAr calorimeters for both electromagnetic and hadronic measurements. The muon spectrometer has separate trigger and high-precision tracking chambers which provide trigger coverage for $|\eta| < 2.4$ and muon identification and momentum measurements for $|\eta| < 2.7$.

¹ATLAS uses a right-handed coordinate system with the z -axis along the beam pipe. The x -axis points to the centre of the LHC ring and the y -axis points upward. The azimuthal angle ϕ is measured around the beam axis and the polar angle θ is the angle from the beam axis. The pseudorapidity is defined as $\eta = -\ln \tan(\theta/2)$. The distance ΔR in the η – ϕ space is defined as $\Delta R = \sqrt{(\Delta\eta)^2 + (\Delta\phi)^2}$.

3 Trigger and data collection

The data were collected from March to December 2012 at a pp centre-of-mass energy of 8 TeV using several triggers. For the primary search region, a missing transverse momentum trigger was used, which bases the bulk of its rejection on the vector sum of transverse energies deposited in projective trigger towers (each with a size of approximately $\Delta\eta \times \Delta\phi \sim 0.1 \times 0.1$ for $|\eta| < 2.5$; these are larger and less regular in the more forward regions). A more refined calculation based on the vector sum of all calorimeter cells above an energy threshold is made at a later stage in the trigger processing. The trigger required $E_T^{\text{miss}} > 80$ GeV, and is fully efficient for offline calibrated $E_T^{\text{miss}} > 150$ GeV in signal-like events. An integrated luminosity of $\int \mathcal{L} dt = (20.1 \pm 0.6) \text{ fb}^{-1}$ was collected using this trigger. The luminosity uncertainty is derived, following the same methodology as that detailed in ref. [45], from a preliminary calibration of the luminosity scale obtained from beam-separation scans performed in November 2012.

Data samples enriched in the major sources of background were collected with electron or muon triggers, yielding an integrated luminosity of $\int \mathcal{L} dt = (20.3 \pm 0.6) \text{ fb}^{-1}$. The electron trigger selects events based on the presence of clusters of energy in the electromagnetic calorimeter, with a shower shape consistent with that of an electron, a matching track in the tracking system, and a transverse energy (E_T) threshold of 24 GeV. In order to recover some of the efficiency for high- p_T electrons, events were also collected with a single-electron trigger with looser requirements, but with the E_T threshold set to 60 GeV. The muon trigger selects events containing one or more muon candidates based on tracks identified in the muon spectrometer and inner detector. For the single-muon trigger, the p_T threshold was 24 GeV. To recover some of the efficiency for higher- p_T muons, events were also collected with a single-muon trigger with a p_T threshold of 36 GeV but with otherwise looser requirements.

Triggers based on the presence of high- p_T jets were used to collect data samples for the estimation of the multijet and all-hadronic $t\bar{t}$ background. The jet p_T thresholds ranged from 55 to 460 GeV. In order to stay within the bandwidth limits of the trigger system, only a fraction of events passing these triggers were recorded to permanent storage.

4 Simulated event samples and SUSY signal modelling

Samples of simulated events are used for the description of the background and to model the SUSY signal. Top quark pair production where at least one of the top quarks decays to a lepton is simulated with POWHEG-BOX [46]. To improve the agreement between data and simulation, $t\bar{t}$ events are reweighted based on the p_T of the $t\bar{t}$ system; the weights are extracted from the ATLAS measurement of the $t\bar{t}$ differential cross section at 7 TeV, following the methods of ref. [47] but updated to the full 7 TeV dataset. POWHEG-BOX is used to simulate single-top production in the s - and Wt -channels, while AcerMC [48] is used for the t -channel. SHERPA [49] is used for $W + \text{jets}$ and $Z + \text{jets}$ production with up to four additional partons (including heavy-flavour jets) as well as for diboson (WW ,

ZZ and WZ) production. MadGraph [50] generation with up to two additional partons is used for $t\bar{t} + W$ and $t\bar{t} + Z$ production.

The underlying-event model is the ATLAS AUET2B tune [51] of PYTHIA [52] except for the $t\bar{t}$ and single-top samples where the Perugia 2011 C tune [53] is used. The parton distribution function (PDF) sets used for the SM background are CT10 [54] for the POWHEG-BOX $t\bar{t}$ and SHERPA samples, and CTEQ6L1 [55] for the MadGraph, POWHEG-BOX single-top, and AcerMC samples.

For the initial comparison with data, all SM background cross sections are normalized to the results of higher-order calculations when available. The theoretical cross sections for $W + \text{jets}$ and $Z + \text{jets}$ are calculated with DYNNLO [56] with the MSTW 2008 NNLO [57] PDF set. The same ratio of the next-to-next-leading-order (NNLO) to leading-order cross sections is applied to the production of W/Z in association with heavy-flavour jets. The inclusive $t\bar{t}$ cross section is calculated at NNLO, including resummation of next-to-next-to-leading-logarithmic (NNLL) soft gluon terms [58], with Top++ [59] using MSTW 2008 NNLO PDFs. The production cross sections of $t\bar{t}$ in association with W/Z are normalized to NLO cross sections [60, 61]. Approximate NLO+NNLL calculations are used for single-top production cross sections [62–64]. For the diboson cross sections, MCFM [65] with MSTW 2008 NLO PDFs is used.

The signal samples are generated with three different configurations: (1) both top squarks decay via $\tilde{t}_1 \rightarrow t\tilde{\chi}_1^0$, (2) one top squark decays via $\tilde{t}_1 \rightarrow t\tilde{\chi}_1^0$ and the other via $\tilde{t}_1 \rightarrow b\tilde{\chi}_1^\pm \rightarrow bW^{(*)}\tilde{\chi}_1^0$, and (3) both top squarks decay via $\tilde{t}_1 \rightarrow b\tilde{\chi}_1^\pm \rightarrow bW^{(*)}\tilde{\chi}_1^0$. With appropriate weighting of these configurations, the analysis sensitivity as a function of the branching fraction to $t\tilde{\chi}_1^0$ can be assessed. In the samples with a decay to $b\tilde{\chi}_1^\pm \rightarrow bW^{(*)}\tilde{\chi}_1^0$, the mass of $\tilde{\chi}_1^\pm$ is chosen to be twice that of $\tilde{\chi}_1^0$ (motivated by models of gaugino unification). The signal samples are generated in a grid across the plane of top squark and $\tilde{\chi}_1^0$ masses with a grid spacing of 50 GeV across most of the plane. The top squark mass ranges from 200 to 750 GeV. In the samples for which both top squarks decay via $\tilde{t}_1 \rightarrow t\tilde{\chi}_1^0$, the $\tilde{\chi}_1^0$ mass ranges from 1 GeV up to approximately 5 GeV below the kinematic limit. For the samples involving $\tilde{t}_1 \rightarrow b\tilde{\chi}_1^\pm \rightarrow bW^{(*)}\tilde{\chi}_1^0$ decays, the chargino mass ranges from 100 GeV (taking into account the LEP limits [66] on the lightest chargino mass) up to approximately 10 GeV below the \tilde{t}_1 mass.

The signal samples for the scenario where both top squarks decay to a top quark and a neutralino are generated using Herwig++ [67]. The neutralino is fixed to be a pure bino, enhancing the decay of the \tilde{t}_R component of \tilde{t}_1 to a right-handed top quark. Hadronic decays are expected to be less sensitive to such polarization effects; a subset of signal samples generated with top squarks corresponding to the left-handed top quark yielded a $< 5\%$ increase in the signal acceptance. The increase in the acceptance due to the polarization is neglected in this paper. The signal samples with mixed decays are generated using MadGraph. The differences between Herwig++ and MadGraph were evaluated for a few samples and found to be negligible. In these mixed decay samples, the chargino is fixed to be a pure wino, and thus top squark decays into $b\tilde{\chi}_1^\pm$ originate from the \tilde{t}_L component of the top squark. The signal samples for which both squarks decay to $b\tilde{\chi}_1^\pm$ are generated with MadGraph where once again the chargino is fixed to be a pure wino. The

PDF set used for all signal samples is CTEQ6L1.

All signal samples are normalized to cross sections calculated to NLO in the strong coupling constant, adding the resummation of soft gluon emission at next-to-leading-logarithmic accuracy (NLO+ NLL) [28–30]. The nominal cross section and its uncertainty are taken from an envelope of cross-section predictions using different PDF sets and factorization and renormalization scales, as described in ref. [68]. The production cross section ranges from approximately 2 pb to 0.008 pb for a top squark mass of 300 GeV to 700 GeV respectively.

The detector simulation [69] is performed using GEANT4 [70] or a fast simulation framework where the showers in the electromagnetic and hadronic calorimeters are simulated with a parameterized description [71] and the rest of the detector is simulated with GEANT4. The fast simulation was validated against full GEANT4 simulation for several signal points. All samples are produced with a varying number of simulated minimum-bias interactions overlaid on the hard-scattering event to account for multiple pp interactions in the same bunch crossing (pileup). The simulation is reweighted to match the distribution in data, which varies between approximately 10 and 30 interactions in each bunch crossing for this dataset. The overlay also treats the impact of pileup from bunch crossings other than the one in which the event occurred. Corrections are applied to the simulated samples to account for differences between data and simulation for the lepton trigger and reconstruction efficiencies, momentum scale and resolution, and for the efficiency of identifying jets originating from the fragmentation of b -quarks, together with the probability for mis-tagging light-flavour and charm quarks.

5 Physics object reconstruction

The reconstructed primary vertex [72] is required to be consistent with the luminous region and to have at least five associated tracks with $p_T > 400$ MeV; when more than one such vertex is found, the vertex with the largest summed p_T^2 of the associated tracks is chosen.

Jets are constructed from three-dimensional clusters of noise-suppressed calorimeter cells [73] using the anti- k_t algorithm [74–76] with a distance parameter $R = 0.4$ and calibrated with a local cluster weighting algorithm [77]. An area-based correction is applied for energy from additional proton–proton collisions based on an estimate of the pileup activity in a given event using the method proposed in ref. [78]. Jets are calibrated [79] and required to have $p_T > 20$ GeV and $|\eta| < 4.5$. Events containing jets arising from detector noise, cosmic-ray muons, or other non-collision sources are removed from consideration [79]. Once the E_T^{miss} is computed and any ambiguity with electrons or muons is resolved (as described below), signal jets are required to have $p_T > 35$ GeV and $|\eta| < 2.8$. Jets containing a b -quark and within the acceptance of the inner detector ($|\eta| < 2.5$) are identified with an algorithm that exploits both the track impact parameters and secondary vertex information [80]; this algorithm is based on a neural network using the output weights of the IP3D, JetFitter+IP3D, and SV1 algorithms (defined in refs. [81, 82]). The identification of these “ b -tagged jets” has an average efficiency of 70% for jets originating

from the fragmentation of a b -quark in simulated $t\bar{t}$ events, a rejection factor of approximately 150 for light-quark and gluon jets (depending on the p_T of the jet), and a rejection factor of approximately 5 for charm jets.

Electrons, which are reconstructed from energy clusters in the electromagnetic calorimeter matched to a track in the inner detector [83], are required to have $|\eta| < 2.47$, $p_T > 10$ GeV, and must pass a variant of the “loose” selection defined in ref. [83] that was re-optimized for 2012 data. In the case where the separation between an electron candidate and a non- b -tagged jet is $\Delta R < 0.2$, the object is considered to be an electron. If the separation between an electron candidate and any jet satisfies $0.2 < \Delta R < 0.4$, or if the separation between an electron candidate and a b -tagged jet is $\Delta R < 0.2$, the electron is not counted. Muons, which are identified either as a combined track in the muon spectrometer and inner detector systems, or as an inner detector track matched with a muon spectrometer segment [84, 85], are required to have $|\eta| < 2.4$ and $p_T > 10$ GeV. If the separation between a muon and any jet is $\Delta R < 0.4$, the muon is not counted.

The $\mathbf{p}_T^{\text{miss}}$ is the negative vector sum of the p_T of the clusters of calorimeter cells, which are calibrated according to their associated reconstructed object (e.g. preselected jets and electrons), and the p_T of preselected muons. The missing transverse momentum from the tracking system (denoted as $\mathbf{p}_T^{\text{miss,track}}$, with magnitude $E_T^{\text{miss,track}}$) is computed from the vector sum of the reconstructed inner detector tracks with $p_T > 500$ MeV, $|\eta| < 2.5$, in association with the primary vertex in the event.

The requirements on electrons and muons are tightened for the selection of events in background control regions (described in section 7) containing leptons. Electrons are required to pass a variant of the “tight” selection of ref. [83] re-optimized for 2012 data, and are required to satisfy track- and calorimeter-based isolation criteria. The scalar sum of the p_T of tracks within a cone of size $\Delta R = 0.3$ (“track isolation”) around the electron (excluding the electron itself) is required to be less than 16% of the electron p_T . The scalar sum of the E_T of pileup-corrected calorimeter energy deposits within a cone of size $\Delta R = 0.3$ (“calorimeter isolation”) around the electron (again, excluding the electron itself) is required to be less than 18% of the electron p_T . The impact parameter of the electron in the transverse plane with respect to the reconstructed event primary vertex ($|d_0|$) is required to be less than five times the impact parameter uncertainty (σ_{d0}). The impact parameter along the beam direction, $|z_0 \times \sin \theta|$, is required to be less than 0.4 mm. Further isolation criteria on reconstructed muons are also imposed: both the track and calorimeter isolation are required to be less than 12% of the muon p_T . In addition, the requirements $|d_0| < 3\sigma_{d0}$ and $|z_0 \times \sin \theta| < 0.4$ mm are imposed for muon candidates. The lepton p_T requirements vary by background control region, as summarized in tables 5–7 in section 7.

6 Signal region definitions

The search for direct top squark pair production in the all-hadronic channel has a nominal experimental signature of six distinct jets (two of which originate from b -quarks), no reconstructed electrons or muons, and significant E_T^{miss} from the LSPs. The stringent requirement of $E_T^{\text{miss}} > 150$ GeV needed to satisfy the trigger rejects the vast majority of

background from multijet and all-hadronic top quark events. Major background contributions include $t\bar{t}$ and $W + \text{jets}$ events where one W decays via a low-momentum or misreconstructed lepton plus a neutrino; after the event selection described later in the text, approximately 40% of the $t\bar{t}$ background arises from a W decaying to a τ lepton that decays hadronically, while the remainder arises equally from W decays to an electron, muon or leptonically decaying τ . Other important background contributions are $Z + \text{jets}$ and $t\bar{t}+Z$ events where the Z decays via neutrinos that escape detection, and single-top events.

This nominal signature, which is labelled “fully resolved” since all of the top squark decay products are individually reconstructed, is sensitive to a wide range of top squark and LSP masses in both the $\tilde{t} \rightarrow t\tilde{\chi}_1^0$ and $\tilde{t} \rightarrow b\tilde{\chi}_1^\pm, \tilde{\chi}_1^\pm \rightarrow W^{(*)}\tilde{\chi}_1^0$ decay modes. The experimental sensitivity to the $\tilde{t} \rightarrow t\tilde{\chi}_1^0$ decay mode, especially for high top squark masses, is enhanced by also considering a second category of “partially resolved” events with particularly high E_T^{miss} and four or five reconstructed jets. This final state can occur if the top quarks are sufficiently Lorentz-boosted such that their decay products merge, and/or if one or more top decay products is below the reconstruction threshold. The consideration of a third category of events with exactly five jets in the final state but a less stringent E_T^{miss} requirement augments the sensitivity to $\tilde{t} \rightarrow b\tilde{\chi}_1^\pm$ decays, particularly where one of the jets from the decay of the $W^{(*)}$ has low p_T and is not reconstructed.

All three categories of events share common selection criteria including $E_T^{\text{miss}} > 150 \text{ GeV}$, as summarized in table 1. The two highest- p_T signal jets are required to have $p_T > 80 \text{ GeV}$ and two of the signal jets must be b -tagged. Events containing reconstructed electrons or muons with $p_T > 10 \text{ GeV}$ are vetoed (thus, $N_{\text{lep}} = 0$). Events with E_T^{miss} arising from mis-measured jets are rejected by requiring an angular separation between the azimuthal angle (ϕ) of the E_T^{miss} and any of the three highest- p_T jets in the event: $|\Delta\phi(\text{jet}, \mathbf{p}_T^{\text{miss}})| > \pi/5$ radians. Further reduction of such events is achieved by requiring the $\mathbf{p}_T^{\text{miss,track}}$ to be aligned in ϕ with respect to the $\mathbf{p}_T^{\text{miss}}$ calculated from the calorimeter system: $|\Delta\phi(\mathbf{p}_T^{\text{miss}}, \mathbf{p}_T^{\text{miss,track}})| < \pi/3$ radians. A substantial rejection of $t\bar{t}$ background is achieved by requiring that the transverse mass (m_T) calculated from the E_T^{miss} and the b -tagged jet closest in ϕ to the $\mathbf{p}_T^{\text{miss}}$ direction exceeds the top mass, as illustrated in figure 2:

$$m_T^{b,\text{min}} = \sqrt{2 p_T^b E_T^{\text{miss}} [1 - \cos \Delta\phi(\mathbf{p}_T^b, \mathbf{p}_T^{\text{miss}})]} > 175 \text{ GeV}. \quad (6.1)$$

In this and subsequent figures displaying simulated signal distributions, the signal samples represent $\tilde{t}_1\tilde{t}_1^*$ production where both top squarks decay via $\tilde{t}_1 \rightarrow t\tilde{\chi}_1^0$ for $m_{\tilde{t}_1} = 600 \text{ GeV}$ and $m_{\tilde{\chi}_1^0} = 1 \text{ GeV}$, or $\tilde{t}_1\tilde{t}_1^*$ production where one top squark decays via $\tilde{t}_1 \rightarrow t\tilde{\chi}_1^0$ and the other decays via $\tilde{t}_1 \rightarrow b\tilde{\chi}_1^\pm$ in each event, for $m_{\tilde{t}_1} = 400 \text{ GeV}$, $m_{\tilde{\chi}_1^\pm} = 200 \text{ GeV}$, and $m_{\tilde{\chi}_1^0} = 100 \text{ GeV}$.

Beyond these common requirements, the three categories of events are further subdivided and optimized individually to target the neutralino or chargino decay modes and particular top squark mass ranges. The most powerful discriminating variable is the E_T^{miss} resulting from the undetected LSPs; signal regions with higher (lower) E_T^{miss} requirements have increased sensitivity to potential signals where the difference in mass between the top squark and the LSP is large (small). The selection criteria obtained from the simulation-based optimization procedure are described in the following.

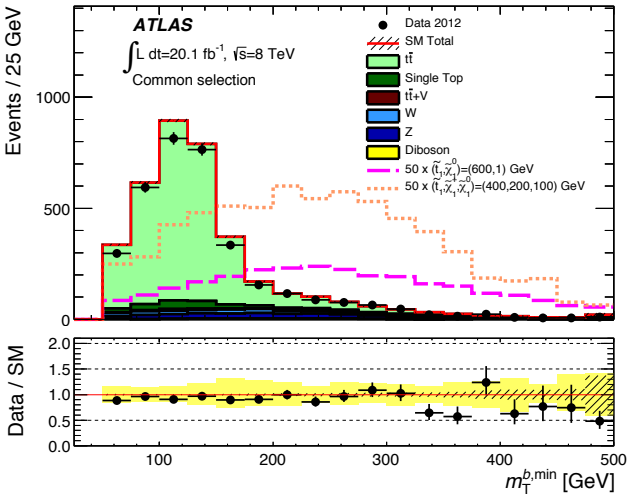


Figure 2. The distribution of $m_T^{b,\min}$ in events with at least four jets that pass the common selection requirements described in the text (see also table 1), excluding the requirement on $m_T^{b,\min}$. The stacked histograms show the SM expectation from simulation compared to the data (points). Simulated signal samples where $m_t = 600$ GeV, $m_{\tilde{\chi}_1^0} = 1$ GeV (pink dashed line) and $m_t = 400$ GeV, $m_{\tilde{\chi}_1^\pm} = 200$ GeV, $m_{\tilde{\chi}_1^0} = 100$ GeV (orange dotted line) are overlaid; the expected number of signal events is multiplied by a factor of 50 for improved visibility. The “Data/SM” plot shows the ratio of data events to the total Standard Model expectation. The rightmost bin includes all overflows. The hatched uncertainty band around the Standard Model expectation shows the statistical uncertainty and the yellow band (shown only for the “Data/SM” plot) shows the combination of statistical and experimental systematic uncertainties.

6.1 Fully resolved signal region (SRA)

This first category of events (SRA) encompasses the nominal signature of six jets plus E_T^{miss} . Events with additional jets from initial- or final-state radiation are also accepted. These events are then divided into four signal regions (SRA1–4) with increasing E_T^{miss} ; the specific requirements are summarized in table 2.

Since all jets from the top quark decays are fully resolved, the two top candidates are reconstructed from signal jets according to the following algorithm. The two jets with the highest b -tagging weight are selected first. From the remaining jets in the event, the two closest jets in the η – ϕ plane are combined to form a W boson candidate; this candidate is then combined with the b -tagged jet closest in the η – ϕ plane to form the first top candidate with mass m_{bjj}^0 . A second W boson candidate is formed by repeating the procedure on the remaining jets; this candidate is then combined with the second of the selected b -tagged jets to form the second top candidate with mass m_{bjj}^1 . The mass requirements on each top candidate are rather loose to ensure high signal efficiency.

Two additional discriminating quantities are introduced to reject the dominant $t\bar{t}$ background in these signal regions. The first quantity, $\min[m_T(\text{jet}^i, \mathbf{p}_T^{\text{miss}})]$, is the minimum value of the transverse mass calculated from each of the signal jets and the $\mathbf{p}_T^{\text{miss}}$, and ensures that the final-state jets are well separated from the $\mathbf{p}_T^{\text{miss}}$. The second quantity is a “ τ

veto" in which events that contain a non- b -tagged jet within $|\eta| < 2.5$ with ≤ 4 associated tracks with $p_T > 500$ MeV, and where the $\Delta\phi$ between the jet and the $\mathbf{p}_T^{\text{miss}}$ is less than $\pi/5$ radians, are vetoed since they are likely to have originated from a $W \rightarrow \tau\nu$ decay.

6.2 Partially resolved signal region targeting $\tilde{t} \rightarrow t\tilde{\chi}_1^0$ decays (SRB)

An alternative top reconstruction algorithm is applied to events with four or five jets in the final state (SRB). The anti- k_t clustering algorithm [74] is applied to $R = 0.4$ signal jets, using reclustered distance parameters of $R = 0.8$ and $R = 1.2$. Nominally, the all-hadronic decay products of a top quark can be reconstructed as three distinct jets, each with a distance parameter of $R = 0.4$. The transverse shape of these jets are typically circular with a radius equal to this distance parameter, but when two of the jets are less than $2R$ apart in η - ϕ space, the one-to-one correspondence of a jet with a top daughter is violated. To some extent, this can be tolerated in the fully resolved scenario without an appreciable efficiency loss, but as the jets become closer together the majority of the p_T is attributed to one of the two jets, and the lower- p_T jet may drop below the minimum p_T requirement. In SRB, at least two reclustered $R = 1.2$ jets are required, and selection criteria are employed based on the masses of these top candidates: $m_{\text{jet}, R=1.2}^0 (m_{\text{jet}, R=1.2}^1)$ is the mass of the highest- p_T (second-highest- p_T) anti- $k_t R = 1.2$ reclustered jet. Requirements are also placed on the p_T of the highest- p_T anti- $k_t R = 1.2$ reclustered jet ($p_{T,\text{jet}, R=1.2}^0$) and the mass of the highest- p_T anti- $k_t R = 0.8$ reclustered jet ($m_{\text{jet}, R=0.8}^0$); this latter requirement rejects background without hadronic W candidates.

For signal regions employing reclustered jets, it is useful to categorize events based on the top mass asymmetry \mathcal{A}_{m_t} , defined as:

$$\mathcal{A}_{m_t} = \frac{|m_{\text{jet}, R=1.2}^0 - m_{\text{jet}, R=1.2}^1|}{m_{\text{jet}, R=1.2}^0 + m_{\text{jet}, R=1.2}^1}. \quad (6.2)$$

Events where $\mathcal{A}_{m_t} < 0.5$ tend to be well balanced, with two well reconstructed top candidates (SRB1). In events where $\mathcal{A}_{m_t} > 0.5$ the top candidates tend to be overlapping or otherwise less well reconstructed (SRB2). Since the two categories of events have markedly different signal-to-background ratios, the selections for these two categories of events are optimized separately.

The background in SRB, which is dominated by $Z + \text{jets}$ and $W + \text{jets}$, is suppressed by requirements on the transverse mass of the $\mathbf{p}_T^{\text{miss}}$ and the non- b -tagged jet closest in $\Delta\phi$ to the $\mathbf{p}_T^{\text{miss}}$, m_T^{\min} , and the transverse mass of the fourth jet (in p_T order) and the $\mathbf{p}_T^{\text{miss}}$, $m_T(\text{jet}^3, \mathbf{p}_T^{\text{miss}})$; this latter variable is used only in four-jet events in SRB1. In SRB2, where the top candidates tend to be less well-reconstructed and background rejection is especially challenging, only five-jet events are considered and an additional requirement is made on a measure of the E_T^{miss} significance: $E_T^{\text{miss}}/\sqrt{H_T}$, where H_T is the scalar sum of the p_T of all five jets in the event. The full set of selection requirements for SRB are detailed in table 3; the logical OR of SRB1 and SRB2 is considered in the final likelihood fit.

Table 1. Selection criteria common to all signal regions.

Trigger	E_T^{miss}
N_{lep}	0
b -tagged jets	≥ 2
E_T^{miss}	$> 150 \text{ GeV}$
$ \Delta\phi(\text{jet}, \mathbf{p}_T^{\text{miss}}) $	$> \pi/5$
$ \Delta\phi(\mathbf{p}_T^{\text{miss}}, \mathbf{p}_T^{\text{miss,track}}) $	$< \pi/3$
$m_T^{b,\text{min}}$	$> 175 \text{ GeV}$

Table 2. Selection criteria for SRA, the fully resolved topology, with ≥ 6 anti- k_t $R = 0.4$ jets.

	SRA1	SRA2	SRA3	SRA4
anti- k_t $R = 0.4$ jets	$\geq 6, p_T > 80, 80, 35, 35, 35, 35 \text{ GeV}$			
m_{bjj}^0	$< 225 \text{ GeV}$	$[50, 250] \text{ GeV}$		
m_{bjj}^1	$< 250 \text{ GeV}$	$[50, 400] \text{ GeV}$		
$\min[m_T(\text{jet}^i, \mathbf{p}_T^{\text{miss}})]$	–	$> 50 \text{ GeV}$		
τ veto	yes			
E_T^{miss}	$> 150 \text{ GeV}$	$> 250 \text{ GeV}$	$> 300 \text{ GeV}$	$> 350 \text{ GeV}$

Table 3. Selection criteria for SRB, the partially resolved topology, with four or five anti- k_t $R = 0.4$ jets, reclustered into anti- k_t $R = 1.2$ and $R = 0.8$ jets.

	SRB1	SRB2
anti- k_t $R = 0.4$ jets	4 or 5, $p_T > 80, 80, 35, 35, (35) \text{ GeV}$	5, $p_T > 100, 100, 35, 35, 35 \text{ GeV}$
\mathcal{A}_{m_t}	< 0.5	> 0.5
$p_{T,\text{jet},R=1.2}^0$	–	$> 350 \text{ GeV}$
$m_{\text{jet},R=1.2}^0$	$> 80 \text{ GeV}$	$[140, 500] \text{ GeV}$
$m_{\text{jet},R=1.2}^1$	$[60, 200] \text{ GeV}$	–
$m_{\text{jet},R=0.8}^0$	$> 50 \text{ GeV}$	$[70, 300] \text{ GeV}$
m_T^{min}	$> 175 \text{ GeV}$	$> 125 \text{ GeV}$
$m_T(\text{jet}^3, \mathbf{p}_T^{\text{miss}})$	$> 280 \text{ GeV}$ for 4-jet case	–
$E_T^{\text{miss}}/\sqrt{H_T}$	–	$> 17\sqrt{H_T} \text{ GeV}$
E_T^{miss}	$> 325 \text{ GeV}$	$> 400 \text{ GeV}$

Table 4. Selection criteria for SRC, targeting the scenario in which one top squark decays via $\tilde{t} \rightarrow b\tilde{\chi}_1^\pm$, with five anti- k_t $R = 0.4$ jets.

	SRC1	SRC2	SRC3
anti- k_t $R = 0.4$ jets	$5, p_T > 80, 80, 35, 35, 35 \text{ GeV}$		
$ \Delta\phi(b, b) $	$> 0.2\pi$		
$m_T^{b,\text{min}}$	$> 185 \text{ GeV}$	$> 200 \text{ GeV}$	$> 200 \text{ GeV}$
$m_T^{b,\text{max}}$	$> 205 \text{ GeV}$	$> 290 \text{ GeV}$	$> 325 \text{ GeV}$
τ veto	yes		
E_T^{miss}	$> 160 \text{ GeV}$	$> 160 \text{ GeV}$	$> 215 \text{ GeV}$

6.3 Signal region targeting $\tilde{t} \rightarrow b\tilde{\chi}_1^\pm$ decays (SRC)

For potential signal events where at least one top squark decays via $\tilde{t} \rightarrow b\tilde{\chi}_1^\pm, \tilde{\chi}_1^\pm \rightarrow W^{(*)}\tilde{\chi}_1^0$, requiring exactly five jets in the final state enhances the sensitivity to smaller values of $m_{\tilde{\chi}_1^\pm} - m_{\tilde{\chi}_1^0}$ at the expense of increased background. Additional discrimination against background where the two b -tagged jets come from a gluon emission is provided by a requirement on $|\Delta\phi(b, b)|$, the azimuthal angle between the two highest- p_T b -tagged jets. To reduce the $t\bar{t}$ background, tighter requirements on $m_T^{b,\min}$ are employed. The quantity $m_T^{b,\max}$ is also used, which is analogous to $m_T^{b,\min}$ except that the transverse mass is computed with the b -tagged jet that has the largest $\Delta\phi$ with respect to the $\mathbf{p}_T^{\text{miss}}$ direction. These two criteria, along with the E_T^{miss} , are tightened in subsequent SRC1–3 sub-regions as summarized in table 4. Finally, the same τ veto as described in section 6.1 is applied.

7 Background estimation

The main background contributions in SRA and SRC arise from $t\bar{t}$ production where one top quark decays semileptonically and the lepton (particularly a hadronically decaying τ lepton) is either not identified or reconstructed as a jet, $Z(\rightarrow v\bar{v})$ plus heavy-flavour jets, and the irreducible background from $t\bar{t}+Z(\rightarrow v\bar{v})$. In SRB, an important contribution comes from W plus heavy-flavour jets, where again the W decays semileptonically and the lepton is reconstructed as a jet or not identified. Other background processes considered are multijets, single top, $t\bar{t}+W$, and diboson production.

With the exception of all-hadronic $t\bar{t}$ and multijet production, all background contributions are estimated primarily from simulation. Control regions (CRs) are used to adjust the normalization of the simulated background contributions in each signal region from semileptonic $t\bar{t}$, $Z \rightarrow v\bar{v}$ plus heavy-flavour jets and, in the case of SRB, W plus heavy-flavour jets. The all-hadronic $t\bar{t}$ and multijet contributions are estimated from data alone in a multijet control region. The control regions are designed to be orthogonal to the signal regions while enhancing a particular source of background; they are used to normalize the simulation for that background to data. The control regions are chosen to be kinematically close to the corresponding signal region, to minimize the systematic uncertainty associated with extrapolating the background yield from the control region to the signal region, but also to have enough data events to avoid a large statistical uncertainty in the background estimate. In addition, control region selections are chosen to minimize potential contamination from signal in the scenarios considered. As the control regions are not always pure in the process of interest, simulation is used to estimate the cross contamination between control regions; the normalization factors and the cross contamination are determined simultaneously for all regions using a fit described in section 7.5.

The selection requirements for all control regions used in this analysis are summarized in tables 5, 6, and 7 for SRA, SRB, and SRC, respectively.

7.1 $t\bar{t}$ background

The control region for the semileptonic $t\bar{t}$ background is defined with requirements similar to those described in section 6 for the top squark signal candidates; however, in order

Table 5. Selection criteria for control regions associated with SRA. Only the requirements that differ from the common selection in table 1 and those in table 2 are listed; “same” indicates the same selection as the signal region.

	$t\bar{t}$ CR	$Z + \text{jets}$ CR	Multijet CR
Trigger	electron (muon)	electron (muon)	same
N_{lep}	1	2	same
p_T^ℓ	$> 35(35)$ GeV	$> 25(25)$ GeV	–
$p_T^{\ell_2}$	same	$> 10(10)$ GeV	same
$m_{\ell\ell}$	–	[86, 96] GeV	–
$E_T^{\text{miss,track}}$	–	–	same
$ \Delta\phi(\mathbf{p}_T^{\text{miss}}, \mathbf{p}_T^{\text{miss,track}}) $	–	–	–
$ \Delta\phi(\text{jet}, \mathbf{p}_T^{\text{miss}}) $	$> \pi/10$	–	< 0.1
$m_T^{b,\min}$	> 125 GeV	–	–
$m_T(\ell, \mathbf{p}_T^{\text{miss}})$	[40, 120] GeV	–	–
$\min[m_T(\text{jet}^l, \mathbf{p}_T^{\text{miss}})]$	–	–	–
m_{bjj}^0 or m_{bjj}^1	< 600 GeV	–	–
E_T^{miss}	> 150 GeV	< 50 GeV	> 150 GeV
$(E_T^{\text{miss}})'$	–	> 70 GeV	–

to enhance the contribution from the semileptonic $t\bar{t}$ process, the events are required to be based on the single-electron or single-muon trigger and to contain a single isolated electron or muon as described in section 5. The transverse mass of the lepton and E_T^{miss} is required to be close to the W mass, namely between 40 and 120 GeV. Events with an additional isolated electron or muon with transverse momentum greater than 10 GeV are rejected. The identified lepton is then treated as a non- b -tagged jet before imposing the jet and b -tagged jet multiplicity requirements. Several signal region requirements are relaxed (or not applied at all) in order to have enough events, while keeping systematic uncertainties related to extrapolating the background yield from the control region to the signal region under control. Figure 3 compares several distributions in data and simulation in the semileptonic $t\bar{t}$ control region for each signal region; the background expectations are normalized using the factors summarized in table 8.

7.2 $W + \text{jets}$ background

For SRB only, a control region is defined for the normalization of the $W + \text{jets}$ background. The control region requirements are similar to those in the $t\bar{t}$ control region for SRB but a number of requirements are changed in order to enhance the W plus heavy-flavour jets process over $t\bar{t}$. The top mass asymmetry in eq. 6.2 is restricted to the region $\mathcal{A}_{m_t} < 0.5$, the number of b -tagged jets is required to be exactly one, and the mass of the leading anti- k_t , $R = 1.2$ reclustered jet is required to be less than 40 GeV. The full list of requirements can be found in table 6. The lepton is treated as a non- b -tagged jet (in a similar fashion as the $t\bar{t}$ control region) before imposing the jet and b -tagged jet multiplicity requirements.

Table 6. Selection criteria for control regions associated with SRB. Only the requirements that differ from the common selection in table 1 and those in table 3 are listed; “same” indicates the same selection as the signal region.

	$t\bar{t}$ CR	$W+\text{jets}$ CR	$Z+\text{jets}$ CR	Multijet CR
Trigger	electron (muon)	electron (muon)	electron (muon)	same
N_{lep}	1	1	2	same
p_T^ℓ	$> 35(35)$ GeV	$> 35(35)$ GeV	$> 25(25)$ GeV	–
$p_T^{f_2}$	same	same	$> 10(10)$ GeV	same
$m_{\ell\ell}$	–	–	[86, 96] GeV	–
anti- $k_t R = 0.4$ jets	[4,5]	[4,5]	5	same
p_T^{jet}	$> 80, 80, 35, 35, (35)$ GeV			same
$N_{b\text{-jet}}$	same	1	same	same
$E_T^{\text{miss,track}}$	–	–	–	same
$ \Delta\phi(p_T^{\text{miss}}, p_T^{\text{miss,track}}) $	–	–	–	–
$ \Delta\phi(\text{jet}, p_T^{\text{miss}}) $	$> \pi/10$	$> \pi/10$	–	< 0.1
m_T^b, \min	–	–	–	–
$m_T(\ell, p_T^{\text{miss}})$	[40, 120] GeV	[40, 120] GeV	–	–
E_T^{miss}	> 150 GeV	> 150 GeV	< 50 GeV	> 150 GeV
$(E_T^{\text{miss}})'$	–	–	> 70 GeV	–
$p_{T,\text{jet}, R=1.2}^0$	–	–	–	–
m_T^{\min}	–	–	–	–
$m_T(\text{jet}^3, p_T^{\text{miss}})$	–	–	–	–
\mathcal{A}_{m_t}	< 0.5 for 4-jet case	< 0.5	–	–
$m_{\text{jet}, R=1.2}^0$	–	< 40 GeV	–	–
$m_{\text{jet}, R=1.2}^1$	–	–	–	–
$m_{\text{jet}, R=0.8}^0$	–	–	–	–
$E_T^{\text{miss}}/\sqrt{H_T}$	–	–	–	–

Table 7. Selection criteria for control regions associated with SRC. Only the requirements that differ from the common selection in table 1 and those in table 4 are listed; “same” indicates the same selection as the signal region.

	$t\bar{t}$ CR	$Z + \text{jets}$ CR	Multijet CR
Trigger	electron (muon)	electron (muon)	same
N_{lep}	1	2	same
p_T^ℓ	$> 35(35)$ GeV	$> 25(25)$ GeV	–
$p_T^{f_2}$	same	$> 10(10)$ GeV	same
$m_{\ell\ell}$	–	[86, 96] GeV	–
$E_T^{\text{miss,track}}$	–	–	same
$ \Delta\phi(p_T^{\text{miss}}, p_T^{\text{miss,track}}) $	–	–	–
$ \Delta\phi(\text{jet}, p_T^{\text{miss}}) $	$> \pi/10$	–	< 0.1
$ \Delta\phi(b, b) $	same	–	–
$m_T^{b, \min}$	> 150 GeV	–	–
$m_T^{b, \max}$	> 125 GeV	–	–
$m_T(\ell, p_T^{\text{miss}})$	[40, 120] GeV	–	–
E_T^{miss}	> 100 GeV	< 50 GeV	> 150 GeV
$(E_T^{\text{miss}})'$	–	> 70 GeV	–

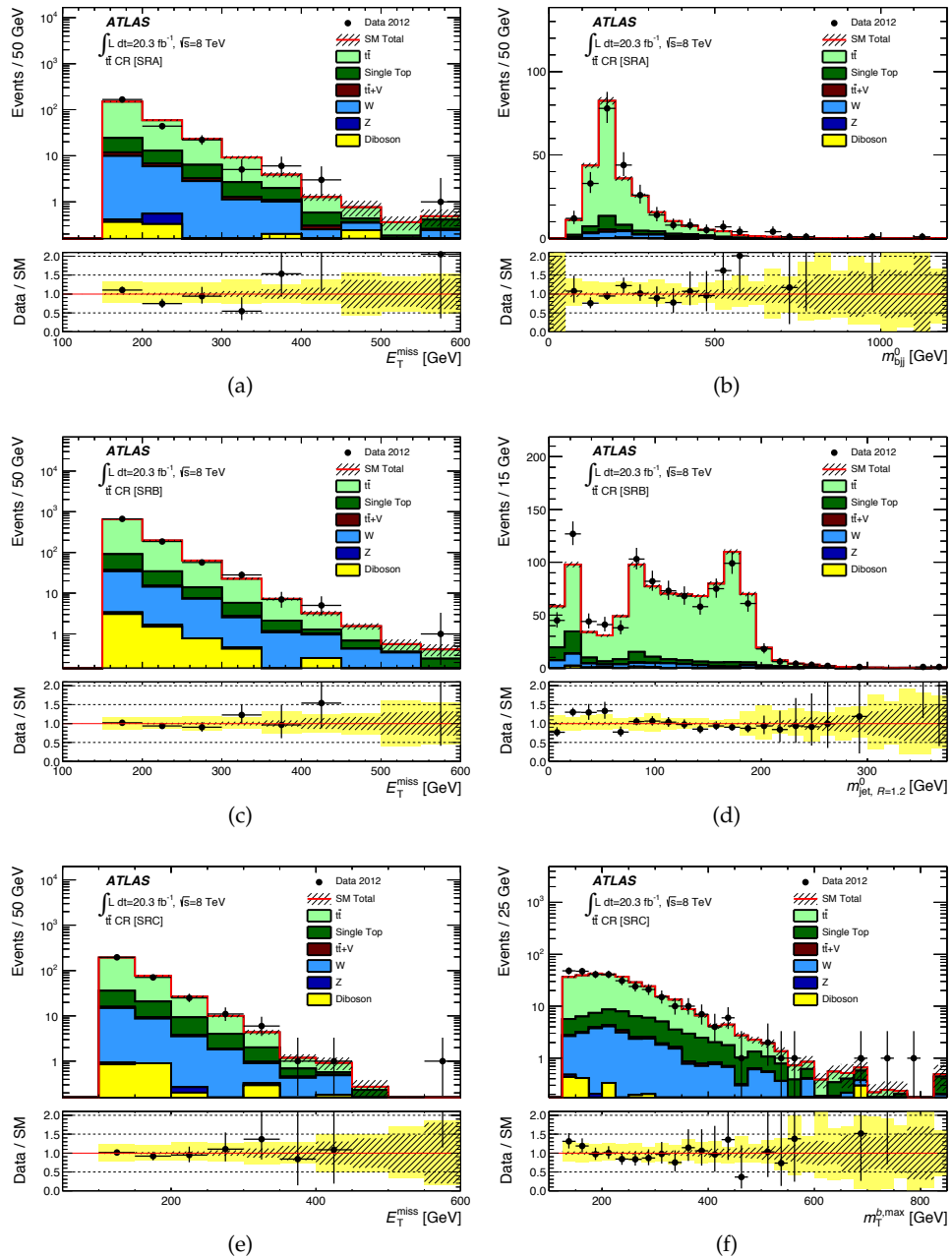


Figure 3. Distributions in the semileptonic $t\bar{t}$ control region of (a) E_T^{miss} and (b) m_{bjj}^0 for SRA, (c) E_T^{miss} and (d) $m_{\text{jet},R=1.2}^0$ for SRB, and (e) E_T^{miss} and (f) $m_T^{b,\text{max}}$ for SRC after the application of all selection requirements. All kinematic quantities were recalculated after treating the lepton as a jet. The stacked histograms show the Standard Model expectation, normalized using the factors summarized in table 8. The “Data/SM” plots show the ratio of data events to the total Standard Model expectation. The rightmost bin includes all overflows. The hatched uncertainty band around the Standard Model expectation shows the statistical uncertainty and the yellow band (shown only for the “Data/SM” plots) shows the combination of statistical and detector-related systematic uncertainties.

Figure 4 shows the E_T^{miss} and $m_T^{b,\text{min}}$ distributions in this control region; the background expectations are normalized using the factors summarized in table 8.

7.3 $Z + \text{jets}$ background

The control region for $Z(\rightarrow v\bar{v})$ plus heavy-flavour jets background is based on a sample of $Z(\rightarrow \ell\ell) + \text{jets}$ events (where ℓ denotes either an electron or muon). The events are collected with the single-lepton triggers. Exactly two oppositely charged electrons or muons are required; the higher- p_T lepton must satisfy $p_T^\ell > 25$ GeV and the lower- p_T lepton must satisfy $p_T^{\ell_2} > 10$ GeV. The invariant mass of the dilepton pair ($m_{\ell\ell}$) is required to be between 86 and 96 GeV. To reduce the $t\bar{t}$ contamination, the events are required to have $E_T^{\text{miss}} < 50$ GeV. The reconstructed dileptons are then removed from the event to mimic the $Z(\rightarrow v\bar{v})$ decay and the vector sum of their momenta is added to the $\mathbf{p}_T^{\text{miss}}$; the events are required to have a recalculated $(E_T^{\text{miss}})' > 70$ GeV. No requirements are made on the number of b -tagged jets. Monte Carlo studies indicate that the E_T^{miss} in $Z + \text{jets}$ events (with $Z(\rightarrow v\bar{v})$) is completely dominated by the neutrinos from the Z decay, independent of the presence of b -tagged jets. The shape of the $(E_T^{\text{miss}})'$ distribution, comparing data to simulation, is shown in figure 5(a); the normalization of the simulation for the estimation of the background is described below.

The fraction of events containing two or more b -tagged jets (henceforth denoted the $b\bar{b}$ -fraction) is found in simulation and data to scale linearly with the number of jets in the event as shown in figure 5(b), as expected when the primary source of b -tagged jet pairs is gluon radiation followed by splitting. The number of events in the $Z + \text{jets}$ control region is corrected in each jet multiplicity bin in simulation and data by the $b\bar{b}$ -fraction. The $b\bar{b}$ -fraction is fit to a linear function of jet multiplicity, starting at a jet multiplicity of two, in order to improve the statistical accuracy for high jet-multiplicity Z events. After correcting for the $b\bar{b}$ -fraction, the $Z + \text{jets}$ simulation is normalized to the data in the control region.

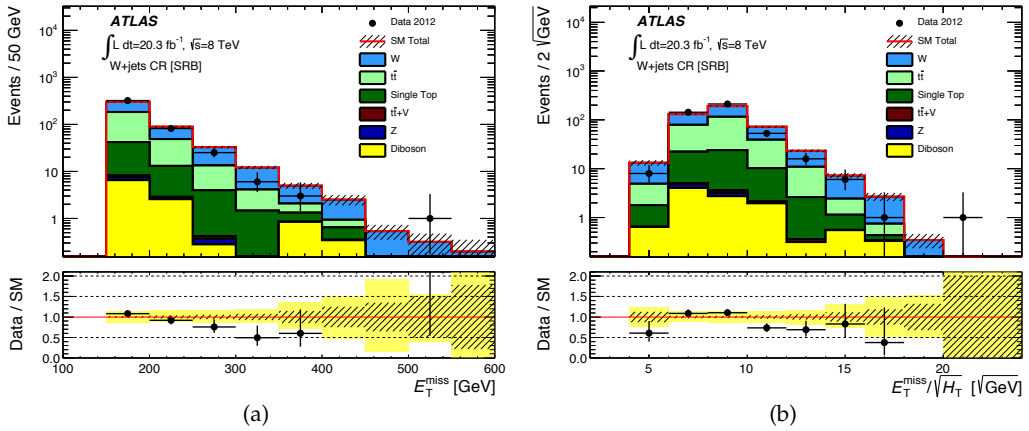


Figure 4. The (a) E_T^{miss} and (b) $E_T^{\text{miss}}/\sqrt{H_T}$ distributions in the $W + \text{jets}$ control region after all selection requirements. All kinematic quantities were recalculated after treating the lepton as a jet. The stacked histograms show the Standard Model expectation, normalized using the factors summarized in table 8. The “Data/SM” plots show the ratio of data events to the total Standard Model expectation. The rightmost bin includes all overflows. The hatched uncertainty band around the Standard Model expectation shows the statistical uncertainty and the yellow band (shown only for the “Data/SM” plots) shows the combination of statistical and detector-related systematic uncertainties.

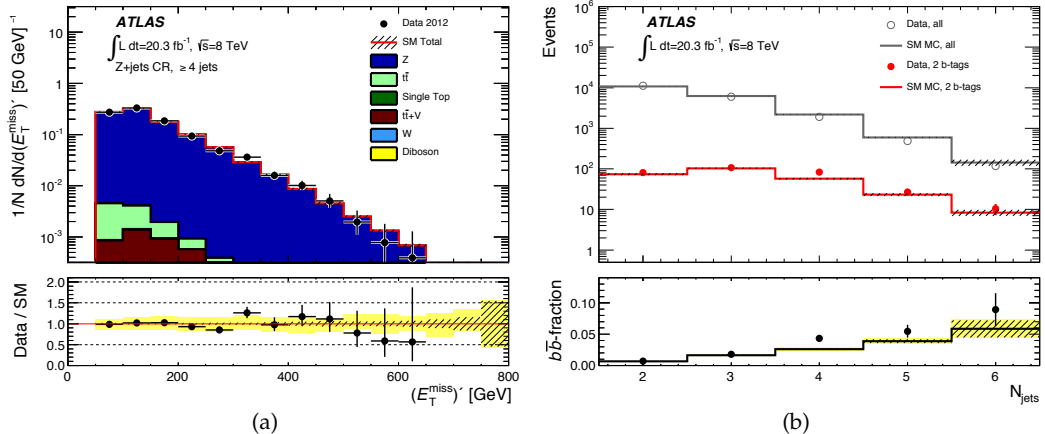


Figure 5. (a) The $(E_T^{\text{miss}})'$ distribution in the $Z + \text{jets}$ control region after all selection requirements for ≥ 4 jets, normalized to unit area. The stacked histograms show the Standard Model expectations. The “Data/SM” plot shows the ratio of data events to the total Standard Model expectation. The rightmost bin includes all overflows. The hatched uncertainty band around the Standard Model expectation shows the statistical uncertainty and the yellow band (shown only for the “Data/SM” plots) shows the combination of statistical and detector-related systematic uncertainties. (b) The number of events in data and simulation as a function of jet multiplicity. The open (solid) points show all events (events with two or more b -tagged jets) in data, while the grey (red) line indicates the SM expectation for all events (events with two or more b -tagged jets). The $b\bar{b}$ -fraction in data (simulation) is shown in the bottom panel, as indicated by the points (line). The hatched areas indicate MC statistical uncertainties and the yellow band (shown only for the $b\bar{b}$ -fraction) includes the b -tagging systematic uncertainty. The rightmost bin includes all overflows.

7.4 Multijet background

The multijet (including fully hadronic $t\bar{t}$) background is evaluated using the jet-smearing technique described in ref. [86]. The basic concept is to take a sample of well-measured multijet events in the data (based on low values of $E_T^{\text{miss}}/\sqrt{\Sigma E_T}$, where ΣE_T is the scalar sum of the transverse energy in the event recorded in the calorimeter systems) and to smear the jet momentum and ϕ direction with jet response functions, determined with PYTHIA8 [87] and corrected with data, separately for light-flavour and heavy-flavour jets. This sample of smeared events is normalized to the data in a control region enriched in multijet events. The same jet multiplicity requirements are applied as in the signal regions, including the requirement of two or more b -tagged jets. The calorimeter-based (track-based) E_T^{miss} is required to be greater than 150 (30) GeV. The signal region requirement on the azimuthal separation $|\Delta\phi(\text{jet}, \mathbf{p}_T^{\text{miss}})|$ is inverted to enhance the population of mis-measured multijet events. Figure 6 compares the $|\Delta\phi(\text{jet}, \mathbf{p}_T^{\text{miss}})|$ and E_T^{miss} distributions in data with expectations in the multijet control region, after normalizing the smeared event sample to the data in the region $|\Delta\phi(\text{jet}, \mathbf{p}_T^{\text{miss}})| < 0.1$. The multijet and fully hadronic $t\bar{t}$ background contributions in the signal regions are evaluated by applying all the signal region requirements to the normalized smeared event sample.

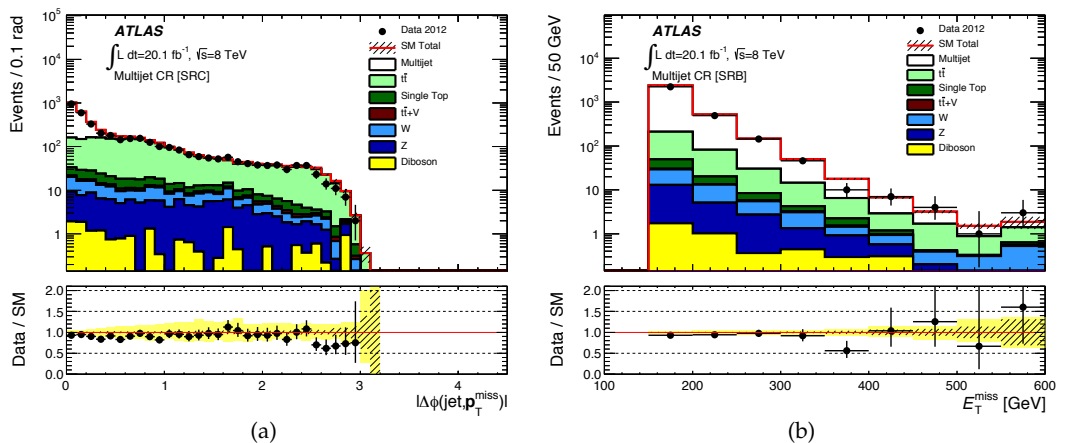


Figure 6. Distributions of (a) $|\Delta\phi(\text{jet}, \mathbf{p}_T^{\text{miss}})|$ in the multijet control region for SRC and (b) E_T^{miss} in the multijet control region for SRB. The stacked histograms show the Standard Model expectations, normalized using the factors summarized in table 8. The “Data/SM” plots show the ratio of data events to the total Standard Model expectation. The rightmost bin includes all overflows. The hatched uncertainty band around the Standard Model expectation shows the statistical uncertainty and the yellow band (shown only for the “Data/SM” plots) shows the combination of statistical and detector-related systematic uncertainties.

Table 8. Normalization of the $t\bar{t}$, $W + \text{jets}$, and $Z + \text{jets}$ SM background as obtained from the background fits for SRA, SRB and SRC.

Background Source	SRA	SRB	SRC
$t\bar{t}$	1.24 ± 0.13	$1.00^{+0.10}_{-0.05}$	1.07 ± 0.11
$W + \text{jets}$	–	1.0 ± 0.4	–
$Z + \text{jets}$	$0.94^{+0.16}_{-0.15}$	1.07 ± 0.07	1.07 ± 0.07

7.5 Simultaneous fit to determine SM background

The observed numbers of events in the various control regions are included in a profile likelihood fit to determine the SM background estimates in each signal region. This procedure takes common systematic uncertainties (discussed in detail in section 8) between the control and signal regions and their correlations into account; they are treated as nuisance parameters in the fit and are modelled by Gaussian probability density functions. For SRA and SRC, the free parameters in the fit are the overall normalizations of the $t\bar{t}$, $Z + \text{jets}$, and multijet background.² For SRB the normalization of the $W + \text{jets}$ background is also a free parameter. The contributions from all other background processes are fixed at the values expected from the simulation, using the most accurate theoretical cross sections available, as described in section 4. The fit to the control regions yields normalization factors for each background source; these are summarized in table 8. These normalization factors are correlated between SRB and SRC due to the overlap of the respective control regions; however, these correlations do not affect the final results since SRB and SRC are never statistically combined, as described in section 9. The resulting yields in the control regions (before and after the fit) are summarized in table 9. The contamination due to potential signal events in the control regions is negligible (at most a few per cent).

²As the smeared events for the multijet background are first normalized “by hand” outside the fit to the data in the multijet control region (after correcting for non-multijet background), the additional normalization factor from the fit is not listed in table 8.

Table 9. Event yields in the control regions, before and after the profile likelihood fit. The uncertainties quoted include statistical and systematic contributions. Smaller background contributions from single-top, $t\bar{t} + W/Z$, and diboson production are included in “Others”.

	CRs for SRA			CRs for SRB			CRs for SRC		
	$t\bar{t}$	$Z + \text{jets}$	Multijets	$t\bar{t}$	$W + \text{jets}$	$Z + \text{jets}$	Multijets	$t\bar{t}$	$Z + \text{jets}$
Observed events									
	247	101	592	950	440	499	2082	313	499
Fitted background events									
Total SM	247 ± 16	101 ± 10	593 ± 27	950 ± 40	440 ± 27	499 ± 22	2082 ± 48	313 ± 18	499 ± 22
$t\bar{t}$	197 ± 21	12.6 ± 3.0	109 ± 23	800 ± 50	189 ± 25	46 ± 7	140 ± 14	239 ± 24	49 ± 12
$Z + \text{jets}$	0.28 ± 0.19	73 ± 11	2.5 ± 0.6	0.59 ± 0.16	1.40 ± 0.25	423 ± 25	11.7 ± 1.6	0.18 ± 0.07	420 ± 26
$W + \text{jets}$	20 ± 9	–	4.5 ± 2.2	54 ± 20	190 ± 40	–	18 ± 7	28 ± 12	–
Multijets	–	–	460 ± 40	–	–	–	1890 ± 50	–	–
Others	29 ± 4	15 ± 4	11.8 ± 1.6	93 ± 13	61 ± 8	30 ± 10	22.7 ± 3.0	45 ± 7	30 ± 7
Expected events (before fit)									
$t\bar{t}$	159	10.2	88	800	190	46	140	224	46
$Z + \text{jets}$	0.31	78	2.7	0.55	1.30	394	10.9	0.17	394
$W + \text{jets}$	20	–	4.5	52	180	–	17	28	–
Multijets	–	–	460	–	–	–	2090	–	–
Others	29	15	11.7	93	61	30	22.7	45	30

The background estimates are validated by predicting the background in dedicated regions and comparing to observation. The validation regions are designed to be orthogonal to the control and signal regions while retaining kinematics and event composition close to the SRs but with little contribution from signal in any of the models considered. For SRA, two validation regions are defined. In the first region (VRA1), all of the requirements for SRA1 are applied except for those on the top mass, and the τ veto is inverted. In the second region (VRA2), all of the SRA1 requirements are applied except for those on the top mass, and $m_T^{b,\min}$ is required to be between 125 and 175 GeV. For SRB, the validation region (VRB) is formed from the logical OR of SRB1 and SRB2 except that the E_T^{miss} requirement is loosened to $E_T^{\text{miss}} > 150$ GeV, $m_T^{b,\min}$ is required to be between 100 and 175 GeV, and none of the other transverse mass requirements are applied. For SRC, the validation regions consist of all the SRC1 requirements except that $m_T^{b,\min}$ is required to be between 150 and 185 GeV and $m_T^{b,\max}$ is required to be greater than 125 GeV, and the τ veto is either inverted (VRC1) or applied (VRC2). All five validation regions are dominated by $t\bar{t}$ background. The background yield in each validation region, predicted from the fit to the control regions, is consistent with the observed number of events to within one standard deviation; these results are summarized in table 10.

Table 10. Event yields in the validation regions compared to the background estimates obtained from the profile likelihood fit. The requirements for VRA1–C2 are described in the text. Statistical and systematic uncertainties in the number of fitted background events are shown. Smaller background contributions from multijets, single-top, $t\bar{t} + W/Z$, and diboson production are included in “Others”.

	VRA1	VRA2	VRB	VRC1	VRC2
Observed events					
	158	51	69	103	24
Fitted background events					
Total SM	189 ± 26	50 ± 6	70 ± 19	110 ± 12	21.1 ± 2.9
$t\bar{t}$	170 ± 27	34 ± 7	60 ± 19	93 ± 12	17.3 ± 2.8
$Z + \text{jets}$	4.0 ± 1.1	1.5 ± 0.4	1.5 ± 0.5	6.9 ± 1.5	0.24 ± 0.20
$W + \text{jets}$	2.8 ± 1.2	4.8 ± 2.2	2.1 ± 1.4	3.9 ± 1.8	1.1 ± 0.5
Others	11.8 ± 3.1	9.1 ± 2.2	7.2 ± 2.5	6.7 ± 2.0	2.4 ± 0.7

8 Systematic uncertainties

Systematic uncertainties in the SM background estimates and signal expectations are evaluated and included in the profile likelihood fit described in section 7.5. The impact of each source of systematic uncertainty is quantified as a percentage of the total background estimate (signal expectation) after propagating the uncertainty from the relevant nuisance parameter, keeping all other fit parameters fixed. All correlations with the other parameters of interest are taken into account.

The main sources of detector-related systematic uncertainties in the SM background estimates are the jet energy resolution (JER) and jet energy scale (JES). These jet reconstruction uncertainties are propagated to all quantities that depend on the jet energies such as the reconstructed top mass and the E_T^{miss} . Additional uncertainties in E_T^{miss} that arise from energy deposits unassociated with reconstructed objects are also included. The impact of these uncertainties is mitigated by the normalization of the dominant SM background contributions in the kinematically similar control regions. The JER uncertainty is derived from in-situ measurements of the jet response asymmetry in dijet events [79]; the effect of this uncertainty on the background estimates in the signal regions ranges from 6–15% in SRA, 16% in SRB, and 3–6% in SRC. The JES uncertainty is determined using the techniques described in refs. [79, 88]; the uncertainties are determined in bins of jet η and p_T and depend on jet flavour and the number of primary vertices in an event. The effect of the JES uncertainty on the background estimate ranges from 5–9% in SRA, 6% in SRB, and 8–11% in SRC. Other uncertainties arising from the simulation of b -tagging, pileup, the τ veto, and $E_T^{\text{miss,track}}$ are negligible by comparison.

A 2.8% uncertainty in the luminosity determination [45] is included for all signal and background MC simulations.

Theoretical uncertainties in the modelling of the SM background are evaluated; their impact is mitigated by the use of control regions to normalize the background contributions. For the $t\bar{t}$ background, uncertainties due to the choice of parton shower (PYTHIA vs. HERWIG [89]+JIMMY [90]), the renormalization and factorization scales (each varied up and down by a factor of two), the amount of initial- and final-state radiation (using AcerMC samples with differing parton shower settings, constrained by measurement [91]), and the PDF uncertainties (derived from the envelope of variations of the CT10 PDF summed in quadrature with the difference with respect to the HERA PDFs [92]) are evaluated. The resulting uncertainties in the total background yields are less than 10% in SRA and SRC (the signal regions with an appreciable contribution from $t\bar{t}$ production). For $t\bar{t} + W/Z$ background, the theoretical uncertainty is dominated by the 22% uncertainty [60, 93] on the NLO cross section. Additional variations considered include the choice of renormalization and factorization scales (each varied up and down by a factor of two), the amount of initial- and final-state radiation (using simulated MadGraph samples), and the matching scale at which additional jets from the matrix element are distinguished from those generated by the parton shower. Finally the uncertainty arising from the use of a finite number of additional partons in the matrix element is assessed by comparing event yields from samples with one versus two additional partons in the matrix element. The

resulting impact on the total background yields range from 3–6% in SRA, 6% in SRB, and is at the per cent level in SRC.

Systematic uncertainties in the modelling of the $W +$ jets background are evaluated with respect to the choice of renormalization and factorization scales (each varied up and down by a factor of two), the matching scale, the PDF uncertainties, and event generation with a finite number of partons (comparing samples with four versus five additional partons in the matrix element). An uncertainty of 38% is applied to the $W +$ heavy flavour production cross section; this is derived from the measurement in ref. [94] and extrapolated to events with at least five jets. An additional uncertainty of 20% is applied to the $W +$ jets control region for SRB to account for differing fractions of $W + c$ vs. $W + b\bar{b}/c\bar{c}$ in the control region compared to the signal region. For the $Z +$ jets background, the uncertainties due to the choice of generator (ALPGEN vs. SHERPA), the PDF uncertainties, and event generation with a finite number of partons are evaluated. The resulting impact on the total background yields from all of the above-mentioned $W +$ jets ($Z +$ jets) theoretical uncertainties are 1–2% (1–2%) in SRA, 10% (9%) in SRB, and 5% (4–5%) in SRC. An additional systematic uncertainty of 17% is assigned to the background yield from the uncertainty in the linear fit to the $b\bar{b}$ -fraction in the $Z +$ jets control region described in section 7.3.

The single-top background is dominated by the Wt subprocess; the cross-section uncertainty is taken from ref. [63]. Additional uncertainties are evaluated for the selection of generator (MC@NLO vs. POWHEG-BOX), parton shower, initial- and final-state radiation, and PDF choices. Finally, the effect of the interference between single-top and $t\bar{t}$ production is evaluated from a comparison of the sum of $t\bar{t}$ and single-top background from POWHEG-BOX with the background from an AcerMC sample of the inclusive $WbWb$ final state. The resulting uncertainty in the total background estimate ranges between 1% and 5%, depending on the signal region. An uncertainty of 50% is assigned to diboson production, resulting in uncertainties in the total background yield of < 1% in all signal regions. An uncertainty of 100% is assigned to the small multijet background, with negligible impact on the total background uncertainty.

The theoretical uncertainties in the top squark production cross section include uncertainties due to the chosen PDF, factorization and renormalization scales, and strong coupling constant variations. These uncertainties are not included as nuisance parameters in the fit; instead, their impact is shown explicitly in the results. In contrast, systematic uncertainties in the signal acceptance are included as nuisance parameters in the fit. The impact on the signal acceptance of variations in the PDF, factorization and renormalization scales, and strong coupling constant is found to be negligible. The systematic uncertainty in the signal acceptance due to the modelling of initial-state radiation is negligible in the region where this analysis has sensitivity to top squark production. Detector-related systematic uncertainties in the signal acceptance are dominated by the JES (4–16% effect on the signal yield in SRA, 3% in SRB, 4–10% in SRC), b -tagging (7–8% in all signal regions) uncertainties and JER (2–10% in SRA, 10% in SRB and 2–3% in SRC). All detector-related uncertainties are assumed to be fully correlated with those of the background.

9 Results and interpretation

The numbers of events observed in data in each of the eight signal regions are presented in table 11. These results are compared to the total number of expected background events in each signal region. The total background estimate is determined from the simultaneous fit based on the profile likelihood method [95] using a procedure similar to that described in section 7.5 but including the corresponding signal regions as well as control regions. The E_T^{miss} distributions for each signal region are displayed in figure 7; the distributions for SRA1 and SRA2 as well as SRA3 and SRA4 are combined since they only differ by the E_T^{miss} requirement. In these figures, the background expectations are normalized by the factors given in table 8.

No significant excess above the SM expectation is observed in any of the signal regions. The probabilities are all consistent with the background-only hypothesis; the smallest p_0 value is 0.19 for SRA4. The 95% confidence level (CL) upper limits on the number of beyond-the-SM (BSM) events in each signal region are derived using the CL_s prescription [96] and calculated from asymptotic formulae [95]. Any possible signal contamination in the control regions is neglected. The BSM signal strength is included as a free parameter but constrained to be non-negative. Normalizing the upper limits on the numbers of events by the integrated luminosity of the data sample, they can be interpreted as model-independent limits on the visible BSM cross sections, defined as $\sigma_{\text{vis}} = \sigma \cdot A \cdot \varepsilon$, where σ is the production cross section, A is the acceptance, and ε is the selection efficiency for a BSM signal. Table 11 summarizes these upper limits for each signal region. A comparison between results obtained using pseudo-experiments and the asymptotic approximation was performed; the two methods are found to be in good agreement.

The results from the simultaneous fit to the signal and control regions are used to set limits on direct top squark pair production except that a fixed signal component is used here and any signal contamination in the CRs is taken into account. Again, limits are derived using the CL_s prescription and calculated from asymptotic formulae. By design, SRA is orthogonal to SRB and SRC. However, SRB and SRC are not independent (each considers five-jet events). Therefore each of SRA1–4 is statistically combined both with SRB (SRA+SRB) and with each of SRC1–3 (SRA+SRC). The SRA+SRB or SRA+SRC combination with the smallest expected 95% CL_s value is chosen for each \tilde{t}_1 and $\tilde{\chi}_1^0$ mass. In these combinations, the signal and detector-related systematic uncertainties are treated as correlated while the theoretical uncertainties and those due to the background normalizations in the independent control regions are treated as uncorrelated. ‘Expected’ limits are calculated by setting the nominal event yield in each SR to the mean background expectation; contours that correspond to $\pm 1\sigma$ uncertainties in the background estimates (σ_{exp}) are also evaluated. ‘Observed’ limits for each channel are calculated from the observed event yields in the signal regions for the nominal signal cross sections and $\pm 1\sigma$ theory uncertainties ($\sigma_{\text{theory}}^{\text{SUSY}}$). Numbers quoted in the text are evaluated from the observed exclusion limit based on the nominal cross section minus $1\sigma_{\text{theory}}^{\text{SUSY}}$.

Table 11. Event yields in each signal region (SRA, SRB, and SRC) are compared to the background estimate from the profile likelihood fit. Statistical, detector, and theoretical systematic uncertainties are included; the total systematic uncertainty in the background estimate includes all correlations. For each signal region, the 95% CL upper limits on the expected (observed) visible cross sections $\sigma_{\text{vis}}(\text{exp})$ ($\sigma_{\text{vis}}(\text{obs})$) and the expected (observed) event yields N_{exp}^{95} (N_{obs}^{95}) are summarized.

	SRA1	SRA2	SRA3	SRA4	SRB	SRC1	SRC2	SRC3
Observed events	11	4	5	4	2	59	30	15
Total SM	15.8 ± 1.9	4.1 ± 0.8	4.1 ± 0.9	2.4 ± 0.7	2.4 ± 0.7	68 ± 7	34 ± 5	20.3 ± 3.0
$t\bar{t}$	10.6 ± 1.9	1.8 ± 0.5	1.1 ± 0.6	0.49 ± 0.34	$0.10^{+0.14}_{-0.10}$	32 ± 4	12.9 ± 2.0	6.7 ± 1.2
$t\bar{t} + W/Z$	1.8 ± 0.6	0.85 ± 0.29	0.82 ± 0.29	0.50 ± 0.17	0.47 ± 0.17	3.2 ± 0.8	1.9 ± 0.5	1.3 ± 0.4
$Z + \text{jets}$	1.4 ± 0.5	0.63 ± 0.22	1.2 ± 0.4	0.68 ± 0.27	1.23 ± 0.31	15.7 ± 3.5	9.0 ± 1.9	6.1 ± 1.3
$W + \text{jets}$	1.0 ± 0.5	0.46 ± 0.21	0.21 ± 0.19	$0.06^{+0.10}_{-0.06}$	0.49 ± 0.33	8 ± 4	4.8 ± 2.2	2.8 ± 1.2
Single top	1.0 ± 0.4	0.30 ± 0.17	0.44 ± 0.14	0.31 ± 0.16	0.08 ± 0.06	7.2 ± 2.9	4.5 ± 1.8	2.9 ± 1.4
Diboson	< 0.4	< 0.13	0.32 ± 0.17	0.32 ± 0.18	0.02 ± 0.01	1.1 ± 0.8	$0.6^{+0.7}_{-0.6}$	$0.6^{+0.7}_{-0.6}$
Multijets	< 0.001	< 0.001	< 0.001	< 0.001	< 0.001	0.24 ± 0.24	0.06 ± 0.06	0.01 ± 0.01
$\sigma_{\text{vis}}(\text{obs}) [\text{fb}]$	0.33	0.29	0.33	0.32	0.21	0.78	0.62	0.40
$\sigma_{\text{vis}}(\text{exp}) [\text{fb}]$	$0.48^{+0.21}_{-0.14}$	$0.29^{+0.13}_{-0.09}$	$0.29^{+0.14}_{-0.09}$	$0.25^{+0.13}_{-0.07}$	$0.24^{+0.13}_{-0.06}$	$1.03^{+0.42}_{-0.29}$	$0.73^{+0.31}_{-0.21}$	$0.55^{+0.24}_{-0.15}$
N_{obs}^{95}	6.6	5.7	6.7	6.5	4.2	15.7	12.4	8.0
N_{exp}^{95}	$9.7^{+4.3}_{-3.0}$	$5.8^{+2.6}_{-1.8}$	$5.9^{+2.8}_{-1.9}$	$5.0^{+2.6}_{-1.4}$	$4.7^{+2.6}_{-1.2}$	$20.7^{+8.4}_{-5.8}$	$14.7^{+6.2}_{-4.2}$	$11.0^{+4.9}_{-3.1}$

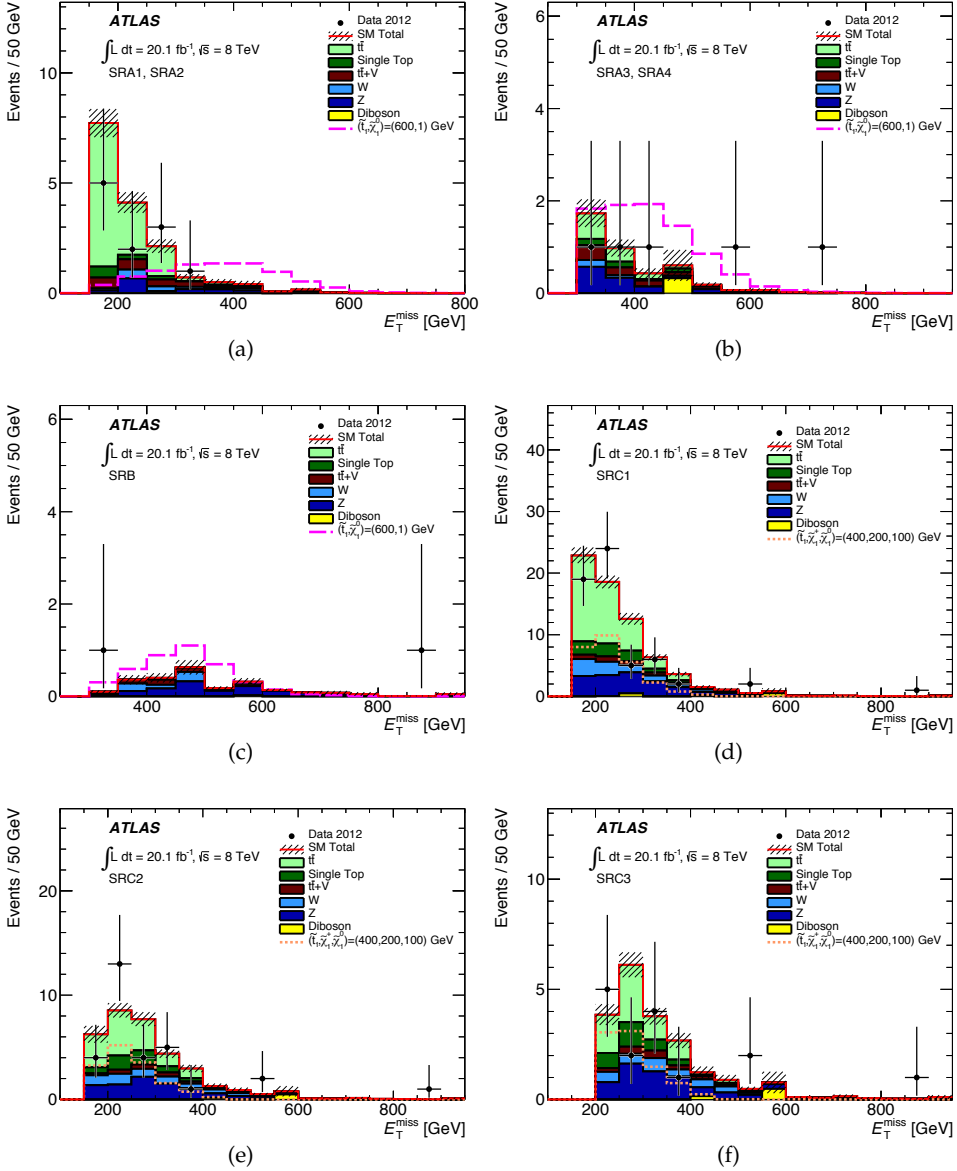


Figure 7. The E_T^{miss} distributions for SRA, SRB, and SRC. SRA1 and SRA2 (SRA3 and SRA4) differ only by the E_T^{miss} requirement. The background expectation (data) are represented by the stacked histogram (black points). For SRA and SRB, the simulated signal distribution for $m_{\tilde{t}} = 600 \text{ GeV}$, $m_{\tilde{\chi}_1^0} = 1 \text{ GeV}$ is overlaid (pink dashed line), while for SRC the simulated signal distribution for $m_{\tilde{t}} = 400 \text{ GeV}$, $m_{\tilde{\chi}_1^{\pm}} = 200 \text{ GeV}$, and $m_{\tilde{\chi}_1^0} = 100 \text{ GeV}$ is overlaid (orange dotted line). The hatched band on the SM total histogram represents the MC statistical uncertainty only.

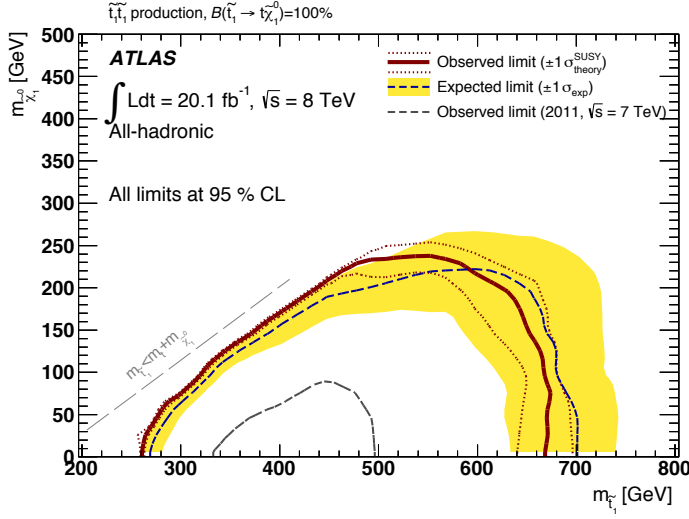


Figure 8. Exclusion contours at 95% CL in the scenario where both top squarks decay exclusively via $\tilde{t} \rightarrow t\tilde{\chi}_1^0$ and the top quark decays hadronically. The blue dashed line indicates the expected limit, and the yellow band indicates the $\pm 1\sigma$ uncertainties, which include all uncertainties except the theoretical uncertainties in the signal. The red solid line indicates the observed limit, and the red dotted lines indicate the sensitivity to $\pm 1\sigma$ variations of the signal theoretical uncertainties. The observed limit from the all-hadronic $\sqrt{s} = 7$ TeV search [32] is overlaid for comparison.

The resulting exclusion contours for the scenario where both top squarks decay via $\tilde{t} \rightarrow t\tilde{\chi}_1^0$ are shown in figure 8, demonstrating an expected sensitivity to potential top squark signals of $275 < m_{\tilde{t}} < 700$ GeV for $m_{\tilde{\chi}_1^0} < 30$ GeV. The combination of SRA1 or SRA2 with SRC1 tends to be most sensitive for smaller $\tilde{t}-\tilde{\chi}_1^0$ mass differences, while the combination of SRA3 or SRA4 with SRB is most sensitive at larger mass differences. Assuming $B(\tilde{t}_1 \rightarrow t\tilde{\chi}_1^0) = 100\%$, top squark masses in the range 270–645 GeV are excluded for $m_{\tilde{\chi}_1^0} < 30$ GeV.

Since the top squark is assumed to decay via either $\tilde{t}_1 \rightarrow t\tilde{\chi}_1^0$ or $\tilde{t}_1 \rightarrow b\tilde{\chi}_1^\pm \rightarrow bW^{(*)}\tilde{\chi}_1^0$, the results are also presented for different values of the branching fraction of $\tilde{t}_1 \rightarrow t\tilde{\chi}_1^0$. The mass of the chargino is assumed to be twice the mass of the neutralino. The resulting exclusion contours are shown in figure 9 (a), demonstrating an expected sensitivity to potential top squark signals of $260 < m_{\tilde{t}} < 565$ GeV for $m_{\tilde{\chi}_1^0} < 60$ GeV and $B(\tilde{t}_1 \rightarrow t\tilde{\chi}_1^0) = 50\%$. The grey filled area corresponds to the $\tilde{\chi}_1^0$ mass region excluded by the LEP limit on the lightest chargino mass, taking into account $m_{\tilde{\chi}_1^\pm} = 2m_{\tilde{\chi}_1^0}$ [66, 97–100]. For $B(\tilde{t}_1 \rightarrow t\tilde{\chi}_1^0) = 50\%$, top squark masses in the range 250–550 GeV are excluded for $m_{\tilde{\chi}_1^0} < 60$ GeV. Figure 9 (b) shows the expected and observed contours for a range of $B(\tilde{t}_1 \rightarrow t\tilde{\chi}_1^0)$ values: 100%, 75%, 50%, 25%, and 0%, where 0% indicates that both top squarks decay exclusively via $\tilde{t} \rightarrow b\tilde{\chi}_1^\pm, \tilde{\chi}_1^\pm \rightarrow W^{(*)}\tilde{\chi}_1^0$. The excluded top squark mass ranges are summarized as a function of $B(\tilde{t}_1 \rightarrow t\tilde{\chi}_1^0)$ in table 12.

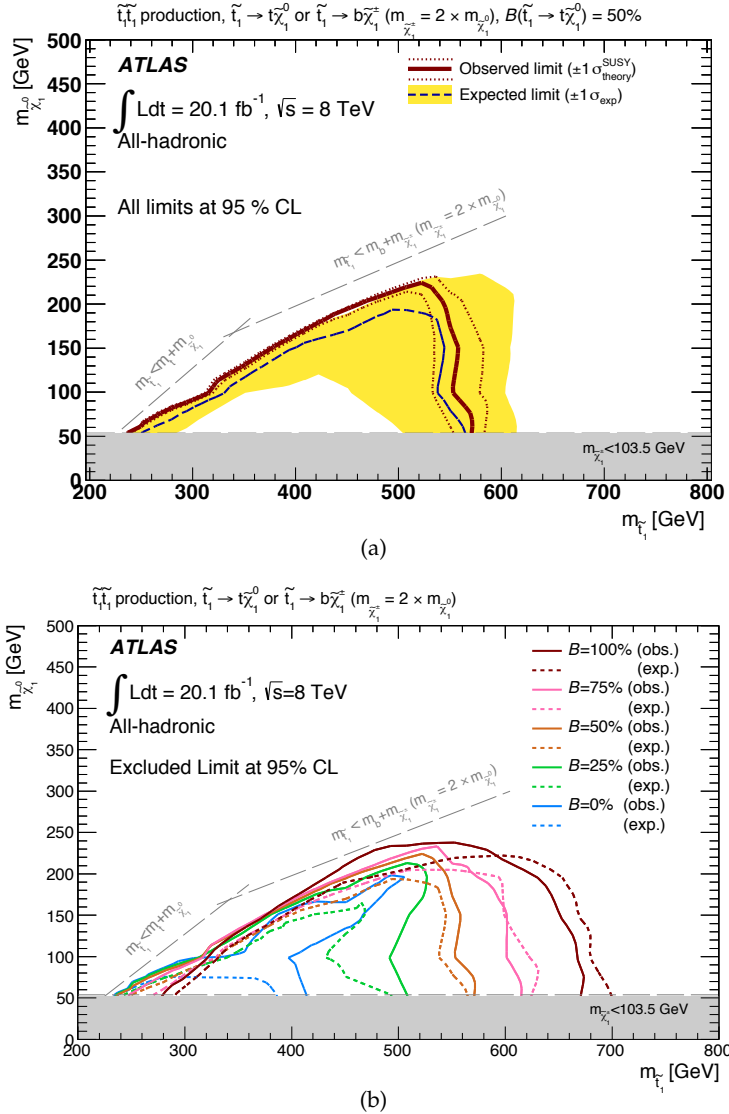


Figure 9. Exclusion contours at 95 % CL in the scenario where the top squarks are allowed to decay via $\tilde{t} \rightarrow b\tilde{\chi}_1^\pm, \tilde{\chi}_1^\pm \rightarrow W^{(*)}\tilde{\chi}_1^0$. The $\tilde{\chi}_1^\pm$ mass is fixed to twice the $\tilde{\chi}_1^0$ mass, and the grey filled areas correspond to the LEP limit of 103.5 GeV on the lightest chargino mass [66, 97–100]. (a) Expected and observed limits for $B(\tilde{t}_1 \rightarrow \tilde{t}\tilde{\chi}_1^0) = 50\%$. The blue dashed line indicates the expected limit, and the yellow band indicates the $\pm 1\sigma$ uncertainties, which include all uncertainties except the theoretical uncertainties in the signal. The red solid line indicates the observed limit, and the red dotted lines indicate the sensitivity to $\pm 1\sigma$ variations of the signal theoretical uncertainties. (b) The observed and expected exclusion contours are shown for $B(\tilde{t}_1 \rightarrow \tilde{t}\tilde{\chi}_1^0)$ values from 0% (inner contours) to 100% (outer contours). For each branching fraction, the observed (solid line) and expected (dashed line) limits are displayed.

Table 12. Excluded top squark masses for a range of $B(\tilde{t}_1 \rightarrow t\tilde{\chi}_1^0)$ values, assuming $m_{\tilde{\chi}_1^\pm} = 2m_{\tilde{\chi}_1^0}$. The excluded mass ranges correspond to the observed limit minus one standard deviation of the uncertainty in the signal cross section (the inner red dotted contour in figure 8, for example).

$B(\tilde{t}_1 \rightarrow t\tilde{\chi}_1^0)$	$m_{\tilde{t}}$	$m_{\tilde{\chi}_1^0}$
0%	245–400 GeV	< 60 GeV
25%	245–485 GeV	< 60 GeV
50%	250–550 GeV	< 60 GeV
75%	265–595 GeV	< 60 GeV
100%	270–645 GeV	< 30 GeV

10 Conclusions

The results of a search for direct top squark production with an all-hadronic experimental signature of jets and missing transverse momentum are presented, using an integrated luminosity of 20.1 fb^{-1} of proton–proton collision data at $\sqrt{s} = 8\text{ TeV}$ collected by the ATLAS detector at the LHC. In this search, the top squark is assumed to decay via $\tilde{t} \rightarrow t\tilde{\chi}_1^0$ or $\tilde{t} \rightarrow b\tilde{\chi}_1^\pm$. In addition to the nominal fully resolved topology that requires at least six jets, the sensitivity of the analysis is increased by including a partially resolved topology (four or five jets). Furthermore, a dedicated signal region requiring exactly five jets augments the sensitivity to top squark decays via $\tilde{t} \rightarrow b\tilde{\chi}_1^\pm$. These three categories of events are statistically combined to provide improved sensitivity to direct top squark production.

No excess over the SM background prediction is observed, and exclusion limits are reported as a function of the top squark and neutralino masses for a range of the branching fractions of $\tilde{t}_1 \rightarrow t\tilde{\chi}_1^0$ from 0–100%. For $B(\tilde{t}_1 \rightarrow t\tilde{\chi}_1^0) = 100\%$, top squark masses in the range 270–645 GeV are excluded for a $m_{\tilde{\chi}_1^0} < 30\text{ GeV}$, while for $B(\tilde{t}_1 \rightarrow t\tilde{\chi}_1^0) = 50\%$ and $m_{\tilde{\chi}_1^\pm} = 2m_{\tilde{\chi}_1^0}$, top squark masses in the range 250–550 GeV are excluded for a $m_{\tilde{\chi}_1^0} < 60\text{ GeV}$. These limits significantly extend previous results.

Acknowledgments

We thank CERN for the very successful operation of the LHC, as well as the support staff from our institutions without whom ATLAS could not be operated efficiently.

We acknowledge the support of ANPCyT, Argentina; YerPhI, Armenia; ARC, Australia; BMWF and FWF, Austria; ANAS, Azerbaijan; SSTC, Belarus; CNPq and FAPE SP, Brazil; NSERC, NRC and CFI, Canada; CERN; CONICYT, Chile; CAS, MOST and NSFC, China; COLCIENCIAS, Colombia; MSMT CR, MPO CR and VSC CR, Czech Republic; DNRF, DNSRC and Lundbeck Foundation, Denmark; EPLANET, ERC and NSRF, European Union; IN2P3-CNRS, CEA-DSM/IRFU, France; GNSF, Georgia; BMBF, DFG, HGF,

MPG and AvH Foundation, Germany; GSRT and NSRF, Greece; ISF, MINERVA, GIF, I-CORE and Benozi yo Center, Israel; INFN, Italy; MEXT and JSPS, Japan; CNRST, Morocco; FOM and NWO, Netherlands; BRF and RCN, Norway; MNiSW and NCN, Poland; GRICES and FCT, Portugal; MNE/IFA, Romania; MES of Russia and ROSATOM, Russian Federation; JINR; MSTD, Serbia; MSSR, Slovakia; ARRS and MIZŠ, Slovenia; DST/NRF, South Africa; MINECO, Spain; SRC and Wallenberg Foundation, Sweden; SER, SNSF and Cantons of Bern and Geneva, Switzerland; NSC, Taiwan; TAEK, Turkey; STFC, the Royal Society and Leverhulme Trust, United Kingdom; DOE and NSF, United States of America.

The crucial computing support from all WLCG partners is acknowledged gratefully, in particular from CERN and the ATLAS Tier-1 facilities at TRIUMF (Canada), NDGF (Denmark, Norway, Sweden), CC-IN2P3 (France), KIT/GridKA (Germany), INFN-CNAF (Italy), NL-T1 (Netherlands), PIC (Spain), ASGC (Taiwan), RAL (UK) and BNL (USA) and in the Tier-2 facilities worldwide.

References

- [1] ATLAS Collaboration, *Observation of a new particle in the search for the Standard Model Higgs boson with the ATLAS detector at the LHC*, *Phys. Lett. B* **716** (2012) 1–29, [[arXiv:1207.7214](https://arxiv.org/abs/1207.7214)].
- [2] CMS Collaboration, *Observation of a new boson at a mass of 125 GeV with the CMS experiment at the LHC*, *Phys. Lett. B* **716** (2012) 30–61, [[arXiv:1207.7235](https://arxiv.org/abs/1207.7235)].
- [3] S. Weinberg, *Implications of Dynamical Symmetry Breaking*, *Phys. Rev. D* **13** (1976) 974–996.
- [4] E. Gildener, *Gauge Symmetry Hierarchies*, *Phys. Rev. D* **14** (1976) 1667–1672.
- [5] S. Weinberg, *Implications of Dynamical Symmetry Breaking: An Addendum*, *Phys. Rev. D* **19** (1979) 1277–1280.
- [6] L. Susskind, *Dynamics of Spontaneous Symmetry Breaking in the Weinberg-Salam Theory*, *Phys. Rev. D* **20** (1979) 2619–2625.
- [7] H. Miyazawa, *Baryon Number Changing Currents*, *Prog. Theor. Phys.* **36** (6) (1966) 1266–1276.
- [8] P. Ramond, *Dual Theory for Free Fermions*, *Phys. Rev. D* **3** (1971) 2415–2418.
- [9] Y. Golfand and E. Likhtman, *Extension of the Algebra of Poincare Group Generators and Violation of p Invariance*, *JETP Lett.* **13** (1971) 323–326.
- [10] A. Neveu and J. H. Schwarz, *Factorizable dual model of pions*, *Nucl. Phys. B* **31** (1971) 86–112.
- [11] A. Neveu and J. H. Schwarz, *Quark Model of Dual Pions*, *Phys. Rev. D* **4** (1971) 1109–1111.
- [12] J. Gervais and B. Sakita, *Field theory interpretation of supergauges in dual models*, *Nucl. Phys. B* **34** (1971) 632–639.
- [13] D. Volkov and V. Akulov, *Is the Neutrino a Goldstone Particle?*, *Phys. Lett. B* **46** (1973) 109–110.
- [14] J. Wess and B. Zumino, *A Lagrangian Model Invariant Under Supergauge Transformations*, *Phys. Lett. B* **49** (1974) 52–54.
- [15] J. Wess and B. Zumino, *Supergauge Transformations in Four-Dimensions*, *Nucl. Phys. B* **70** (1974) 39–50.

- [16] S. Dimopoulos and H. Georgi, *Softly Broken Supersymmetry and SU(5)*, *Nucl. Phys.* **B 193** (1981) 150–162.
- [17] E. Witten, *Dynamical Breaking of Supersymmetry*, *Nucl. Phys.* **B 188** (1981) 513–554.
- [18] M. Dine, W. Fischler, and M. Srednicki, *Supersymmetric Technicolor*, *Nucl. Phys.* **B 189** (1981) 575–593.
- [19] S. Dimopoulos and S. Raby, *Supercolor*, *Nucl. Phys.* **B 192** (1981) 353–368.
- [20] N. Sakai, *Naturalness in Supersymmetric GUTs*, *Z. Phys. C* **11** (1981) 153–157.
- [21] R. Kaul and P. Majumdar, *Cancellation of quadratically divergent mass corrections in globally supersymmetric spontaneously broken gauge theories*, *Nucl. Phys.* **B 199** (1982) 36–58.
- [22] R. Barbieri and G. Giudice, *Upper Bounds on Supersymmetric Particle Masses*, *Nucl. Phys.* **B 306** (1988) 63–76.
- [23] B. de Carlos and J. Casas, *One loop analysis of the electroweak breaking in supersymmetric models and the fine tuning problem*, *Phys. Lett.* **B 309** (1993) 320–328, [[hep-ph/9303291](#)].
- [24] P. Fayet, *Supersymmetry and Weak, Electromagnetic and Strong Interactions*, *Phys. Lett.* **B 64** (1976) 159–162.
- [25] P. Fayet, *Spontaneously Broken Supersymmetric Theories of Weak, Electromagnetic and Strong Interactions*, *Phys. Lett.* **B 69** (1977) 489–494.
- [26] G. R. Farrar and P. Fayet, *Phenomenology of the Production, Decay, and Detection of New Hadronic States Associated with Supersymmetry*, *Phys. Lett.* **B 76** (1978) 575–579.
- [27] P. Fayet, *Relations Between the Masses of the Superpartners of Leptons and Quarks, the Goldstino Couplings and the Neutral Currents*, *Phys. Lett.* **B 84** (1979) 416–420.
- [28] W. Beenakker et al., *Stop production at hadron colliders*, *Nucl. Phys.* **B 515** (1998) 3–14.
- [29] W. Beenakker et al., *Supersymmetric top and bottom squark production at hadron colliders*, *JHEP* **08** (2010) 098, [[arXiv:1006.4771](#)].
- [30] W. Beenakker et al., *Squark and gluino hadroproduction*, *Int. J. Mod. Phys. A* **26** (2011) 2637–2664.
- [31] ATLAS Collaboration, *Search for scalar top quark pair production in natural gauge mediated supersymmetry models with the ATLAS detector in pp collisions at $\sqrt{s} = 7$ TeV*, *Phys. Lett.* **B 715** (2012) 44–60, [[arXiv:1204.6736](#)].
- [32] ATLAS Collaboration, *Search for a supersymmetric partner to the top quark in final states with jets and missing transverse momentum at $\sqrt{s} = 7$ TeV with the ATLAS detector*, *Phys. Rev. Lett.* **109** (2012) 211802, [[arXiv:1208.1447](#)].
- [33] ATLAS Collaboration, *Search for light scalar top quark pair production in final states with two leptons with the ATLAS detector in $\sqrt{s} = 7$ TeV proton-proton collisions*, *Eur. Phys. J. C* **72** (2012) 2237, [[arXiv:1208.4305](#)].
- [34] ATLAS Collaboration, *Search for a heavy top-quark partner in final states with two leptons with the ATLAS detector at the LHC*, *JHEP* **11** (2012) 094, [[arXiv:1209.4186](#)].
- [35] ATLAS Collaboration, *Search for light top squark pair production in final states with leptons and b-jets with the ATLAS detector in $\sqrt{s} = 7$ TeV proton-proton collisions*, *Phys. Lett.* **B 720** (2013) 13–31, [[arXiv:1209.2102](#)].

- [36] **ATLAS** Collaboration, *Search for direct third-generation squark pair production in final states with missing transverse momentum and two b-jets in $\sqrt{s} = 8$ TeV pp collisions with the ATLAS detector*, *JHEP* **10** (2013) 189, [[arXiv:1308.2631](#)].
- [37] **ATLAS** Collaboration, *Search for direct top squark pair production in events with a Z boson, b-jets and missing transverse momentum in $\sqrt{s}=8$ TeV pp collisions with the ATLAS detector*, [arXiv:1403.5222](#).
- [38] **CMS** Collaboration, *Inclusive search for supersymmetry using the razor variables in pp collisions at $\sqrt{s} = 7$ TeV*, *Phys. Rev. Lett.* **111** (2013), no. 8 081802, [[arXiv:1212.6961](#)].
- [39] **CMS** Collaboration, *Search for supersymmetry in final states with missing transverse energy and 0, 1, 2, or at least 3 b-quark jets in 7 TeV pp collisions using the variable α_T* , *JHEP* **01** (2013) 077, [[arXiv:1210.8115](#)].
- [40] **CMS** Collaboration, *Search for supersymmetry in hadronic final states with missing transverse energy using the variables α_T and b-quark multiplicity in pp collisions at 8 TeV*, *Eur. Phys. J. C* **73** (2013) 2568, [[arXiv:1303.2985](#)].
- [41] **CMS** Collaboration, *Search for top-squark pair production in the single-lepton final state in pp collisions at $\sqrt{s} = 8$ TeV*, *Eur. Phys. J. C* **73** (2013) 2677, [[arXiv:1308.1586](#)].
- [42] **CMS** Collaboration, *Search for top squark and higgsino production using diphoton Higgs boson decays*, *Phys. Rev. Lett.* **112** (2014) 161802, [[arXiv:1312.3310](#)].
- [43] **CMS** Collaboration, *Search for top-squark pairs decaying into Higgs or Z bosons in pp collisions at $\sqrt{s} = 8$ TeV*, [arXiv:1405.3886](#).
- [44] **ATLAS** Collaboration, *The ATLAS Experiment at the CERN Large Hadron Collider*, *JINST* **3** (2008) S08003.
- [45] **ATLAS** Collaboration, *Improved luminosity determination in pp collisions at $\sqrt{s} = 7$ TeV using the ATLAS detector at the LHC*, *Eur. Phys. J. C* **73** (2013) 2518, [[arXiv:1302.4393](#)].
- [46] S. Frixione, P. Nason, and C. Oleari, *Matching NLO QCD computations with Parton Shower simulations: the POWHEG method*, *JHEP* **11** (2007) 070, [[arXiv:0709.2092](#)]. For $t\bar{t}$ (single top) production, POWHEG-BOX version 1.0 r2129 is interfaced with PYTHIA 6.427 (6.426).
- [47] **ATLAS** Collaboration, *Measurements of top quark pair relative differential cross-sections with ATLAS in pp collisions at $\sqrt{s} = 7$ TeV*, *Eur. Phys. J. C* **73** (2013) 2261, [[arXiv:1207.5644](#)].
- [48] B. P. Kersevan and E. Richter-Was, *The Monte Carlo event generator AcerMC version 2.0 with interfaces to PYTHIA 6.2 and HERWIG 6.5*, [hep-ph/0405247](#). AcerMC version 3.8 is interfaced with PYTHIA 6.426.
- [49] T. Gleisberg et al., *Event generation with SHERPA 1.1*, *JHEP* **02** (2009) 007, [[arXiv:0811.4622](#)]. SHERPA version 1.4.1.
- [50] J. Alwall et al., *MadGraph 5 : Going Beyond*, *JHEP* **06** (2011) 128, [[arXiv:1106.0522](#)]. MadGraph 5 version 1.3.33 is interfaced with PYTHIA 6.426.
- [51] **ATLAS** Collaboration, *ATLAS tunes of PYTHIA 6 and Pythia 8 for MC11*, *ATL-PHYS-PUB-2011-009* (2011). <http://cdsweb.cern.ch/record/1363300>.
- [52] T. Sjöstrand, S. Mrenna, and P. Z. Skands, *PYTHIA 6.4 Physics and Manual*, *JHEP* **05** (2006) 026, [[hep-ph/0603175](#)].
- [53] P. Z. Skands, *Tuning Monte Carlo generators: The Perugia tunes*, *Phys. Rev. D* **82** (2010) 074018, [[arXiv:1005.3457](#)].

- [54] H.-L. Lai et al., *New parton distributions for collider physics*, *Phys. Rev.* **D 82** (2010) 074024, [[arXiv:1007.2241](#)].
- [55] J. Pumplin et al., *New generation of parton distributions with uncertainties from global QCD analysis*, *JHEP* **07** (2002) 012, [[hep-ph/0201195](#)].
- [56] S. Catani et al., *Vector boson production at hadron colliders: A Fully exclusive QCD calculation at NNLO*, *Phys. Rev. Lett.* **103** (2009) 082001, [[arXiv:0903.2120](#)].
- [57] A. Martin, W. Stirling, R. Thorne, and G. Watt, *Parton distributions for the LHC*, *Eur. Phys. J.* **C 63** (2009) 189–285, [[arXiv:0901.0002](#)].
- [58] M. Cacciari, M. Czakon, M. Mangano, A. Mitov, and P. Nason, *Top-pair production at hadron colliders with next-to-next-to-leading logarithmic soft-gluon resummation*, *Phys. Lett.* **B 710** (2012) 612–622, [[arXiv:1111.5869](#)].
- [59] M. Czakon and A. Mitov, *Top++: A Program for the Calculation of the Top-Pair Cross-Section at Hadron Colliders*, [arXiv:1112.5675](#). Top++ version 2.0.
- [60] J. M. Campbell and R. K. Ellis, *$t\bar{t}W^{+-}$ production and decay at NLO*, *JHEP* **07** (2012) 052, [[arXiv:1204.5678](#)].
- [61] M. Garzelli, A. Kardos, C. Papadopoulos, and Z. Trocsanyi, *Z^0 - boson production in association with a top anti-top pair at NLO accuracy with parton shower effects*, *Phys. Rev.* **D 85** (2012) 074022, [[arXiv:1111.1444](#)].
- [62] N. Kidonakis, *NNLL resummation for s-channel single top quark production*, *Phys. Rev.* **D 81** (2010) 054028, [[arXiv:1001.5034](#)].
- [63] N. Kidonakis, *Two-loop soft anomalous dimensions for single top quark associated production with a W^- or H^-* , *Phys. Rev.* **D 82** (2010) 054018, [[arXiv:1005.4451](#)].
- [64] N. Kidonakis, *Next-to-next-to-leading-order collinear and soft gluon corrections for t-channel single top quark production*, *Phys. Rev.* **D 83** (2011) 091503, [[arXiv:1103.2792](#)].
- [65] J. M. Campbell, R. K. Ellis, and C. Williams, *Vector boson pair production at the LHC*, *JHEP* **07** (2011) 018, [[arXiv:1105.0020](#)].
- [66] LEP SUSY Working Group (ALEPH, DELPHI L3, OPAL), Notes LEPSUSYWG/01-03.1, <http://lepsusy.web.cern.ch/lepsusy/Welcome.html>.
- [67] M. Bähr et al., *Herwig++ Physics and Manual*, *Eur. Phys. J.* **C 58** (2008) 639–707, [[arXiv:0803.0883](#)].
- [68] M. Krämer et al., *Supersymmetry production cross sections in pp collisions at $\sqrt{s} = 7$ TeV*, [arXiv:1206.2892](#).
- [69] ATLAS Collaboration, *The ATLAS Simulation Infrastructure*, *Eur. Phys. J.* **C 70** (2010) 823–874, [[arXiv:1005.4568](#)].
- [70] GEANT4 Collaboration, S. Agostinelli et al., *GEANT4: A simulation toolkit*, *Nucl. Instrum. Meth. A* **506** (2003) 250–303.
- [71] ATLAS Collaboration, *The simulation principle and performance of the ATLAS fast calorimeter simulation FastCaloSim*, ATL-PHYS-PUB-2010-013 (2010). <http://cdsweb.cern.ch/record/1300517>.
- [72] ATLAS Collaboration, *Performance of primary vertex reconstruction in proton-proton collisions at $\sqrt{s} = 7$ TeV in the ATLAS experiment*, ATLAS-CONF-2010-069 (2010). <http://cdsweb.cern.ch/record/1281344>.

- [73] W. Lampl et al., *Calorimeter Clustering Algorithms: Description and Performance*, ATL-LARG-PUB-2008-002 (2008). <http://cdsweb.cern.ch/record/1099735>.
- [74] M. Cacciari, G. P. Salam, and G. Soyez, *The Anti- $k(t)$ jet clustering algorithm*, *JHEP* **04** (2008) 063, [[arXiv:0802.1189](https://arxiv.org/abs/0802.1189)].
- [75] M. Cacciari and G. P. Salam, *Dispelling the N^3 myth for the k_t jet-finder*, *Phys. Lett. B* **641** (2006) 57–61, [[hep-ph/0512210](https://arxiv.org/abs/hep-ph/0512210)].
- [76] M. Cacciari, G. P. Salam, and G. Soyez, *FastJet User Manual*, *Eur. Phys. J. C* **72** (2012) 1896, [[arXiv:1111.6097](https://arxiv.org/abs/1111.6097)].
- [77] C. Issever, K. Borras, and D. Wegener, *An Improved weighting algorithm to achieve software compensation in a fine grained LAr calorimeter*, *Nucl. Instrum. Meth. A* **545** (2005) 803–812, [[physics/0408129](https://arxiv.org/abs/physics/0408129)].
- [78] M. Cacciari and G. P. Salam, *Pileup subtraction using jet areas*, *Phys. Lett. B* **659** (2008) 119–126, [[arXiv:0707.1378](https://arxiv.org/abs/0707.1378)].
- [79] ATLAS Collaboration, *Jet energy measurement with the ATLAS detector in proton-proton collisions at $\sqrt{s} = 7$ TeV*, *Eur. Phys. J. C* **73** (2013) 2304, [[arXiv:1112.6426](https://arxiv.org/abs/1112.6426)].
- [80] ATLAS Collaboration, *Measurement of the b-tag Efficiency in a Sample of Jets Containing Muons with 5 fb^{-1} of Data from the ATLAS Detector*, ATLAS-CONF-2012-043 (2012). <http://cdsweb.cern.ch/record/1435197>.
- [81] ATLAS Collaboration, *Calibrating the b-Tag Efficiency and Mistag Rate in 35 pb^{-1} of Data with the ATLAS Detector*, ATLAS-CONF-2011-089 (2011). <http://cdsweb.cern.ch/record/1356198>.
- [82] ATLAS Collaboration, *Commissioning of the ATLAS high-performance b-tagging algorithms in the 7 TeV collision data*, ATLAS-CONF-2011-102 (2011). <http://cdsweb.cern.ch/record/1369219>.
- [83] ATLAS Collaboration, *Electron performance measurements with the ATLAS detector using the 2010 LHC proton-proton collision data*, *Eur. Phys. J. C* **72** (2012) 1909, [[arXiv:1110.3174](https://arxiv.org/abs/1110.3174)].
- [84] ATLAS Collaboration, *A measurement of the ATLAS muon reconstruction and trigger efficiency using J/ψ decays*, ATLAS-CONF-2011-021 (2011). <http://cdsweb.cern.ch/record/1336750>.
- [85] ATLAS Collaboration, *Muon reconstruction efficiency in reprocessed 2010 LHC proton-proton collision data recorded with the ATLAS detector*, ATLAS-CONF-2011-063 (2011). <http://cdsweb.cern.ch/record/1345743>.
- [86] ATLAS Collaboration, *Search for squarks and gluinos with the ATLAS detector in final states with jets and missing transverse momentum using 4.7 fb^{-1} of $\sqrt{s} = 7$ TeV proton-proton collision data*, *Phys. Rev. D* **87** (2013) 012008, [[arXiv:1208.0949](https://arxiv.org/abs/1208.0949)].
- [87] T. Sjöstrand, S. Mrenna, and P. Z. Skands, *A Brief Introduction to PYTHIA 8.1*, *Comput. Phys. Commun.* **178** (2008) 852–867, [[arXiv:0710.3820](https://arxiv.org/abs/0710.3820)].
- [88] ATLAS Collaboration, *Single hadron response measurement and calorimeter jet energy scale uncertainty with the ATLAS detector at the LHC*, *Eur. Phys. J. C* **73** (2013) 2305, [[arXiv:1203.1302](https://arxiv.org/abs/1203.1302)].
- [89] G. Corcella et al., *HERWIG 6.5 release note*, [hep-ph/0210213](https://arxiv.org/abs/hep-ph/0210213).
- [90] J. Butterworth, J. R. Forshaw, and M. Seymour, *Multiparton interactions in photoproduction at HERA*, *Z. Phys. C* **72** (1996) 637–646, [[hep-ph/9601371](https://arxiv.org/abs/hep-ph/9601371)].

- [91] **ATLAS** Collaboration, *Measurement of $t\bar{t}$ production with a veto on additional central jet activity in pp collisions at $\sqrt{s} = 7$ TeV using the ATLAS detector*, *Eur. Phys. J. C* **72** (2012) 2043, [[arXiv:1203.5015](#)].
- [92] **H1** and **ZEUS** Collaborations, *Combined Measurement and QCD Analysis of the Inclusive $e^\pm p$ Scattering Cross Sections at HERA*, *JHEP* **01** (2010) 109, [[arXiv:0911.0884](#)].
- [93] M. Garzelli, A. Kardos, C. Papadopoulos, and Z. Trocsanyi, *$t\bar{t}W^\pm$ and $t\bar{t}Z$ Hadroproduction at NLO accuracy in QCD with Parton Shower and Hadronization effects*, *JHEP* **11** (2012) 056, [[arXiv:1208.2665](#)].
- [94] **ATLAS** Collaboration, *Measurement of the cross-section for W boson production in association with b -jets in pp collisions at $\sqrt{s} = 7$ TeV with the ATLAS detector*, *J. High Energy Phys.* **06** (2013) 084, [[arXiv:1302.2929](#)].
- [95] G. Cowan, K. Cranmer, E. Gross, and O. Vitells, *Asymptotic formulae for likelihood-based tests of new physics*, *Eur. Phys. J. C* **71** (2011) 1554, [[arXiv:1007.1727](#)].
- [96] A. L. Read, *Presentation of search results: The $CL(s)$ technique*, *J. Phys. G* **28** (2002) 2693–2704.
- [97] **ALEPH** Collaboration, A. Heister et al., *Absolute mass lower limit for the lightest neutralino of the MSSM from e^+e^- data at \sqrt{s} up to 209 GeV*, *Phys. Lett. B* **583** (2004) 247–263.
- [98] **DELPHI** Collaboration, J. Abdallah et al., *Searches for supersymmetric particles in e^+e^- collisions up to 208 GeV and interpretation of the results within the MSSM*, *Eur. Phys. J. C* **31** (2003) 421–479, [[hep-ex/0311019](#)].
- [99] **L3** Collaboration, M. Acciarri et al., *Search for charginos and neutralinos in e^+e^- collisions at $\sqrt{s} = 189$ GeV*, *Phys. Lett. B* **472** (2000) 420–433, [[hep-ex/9910007](#)].
- [100] **OPAL** Collaboration, G. Abbiendi et al., *Search for chargino and neutralino production at $\sqrt{s} = 192$ GeV to 209 GeV at LEP*, *Eur. Phys. J. C* **35** (2004) 1–20, [[hep-ex/0401026](#)].

EUROPEAN ORGANISATION FOR NUCLEAR RESEARCH (CERN)



CERN-PH-EP-2014-112

arXiv: 1406.1122 [hep-ex]

Auxiliary figures and tables from the paper

Search for direct pair production of the top squark in all-hadronic final states in proton–proton collisions at $\sqrt{s} = 8$ TeV with the ATLAS detector

The ATLAS Collaboration

SUSY-2013-16

This document contains auxiliary figures and tables from the paper:

“Search for direct pair production of the top squark in all-hadronic final states in proton–proton collisions at $\sqrt{s} = 8$ TeV with the ATLAS detector”.

All figures can be found at:

<https://atlas.web.cern.ch/Atlas/GROUPS/PHYSICS/PAPERS/SUSY-2013-16>

The information is uploaded to HepData in the record:

<http://hepdata.cedar.ac.uk/view/ins1299143>,

where details about the models used in the paper, the selections and the final fit results can be found.

© 2014 CERN for the benefit of the ATLAS Collaboration.

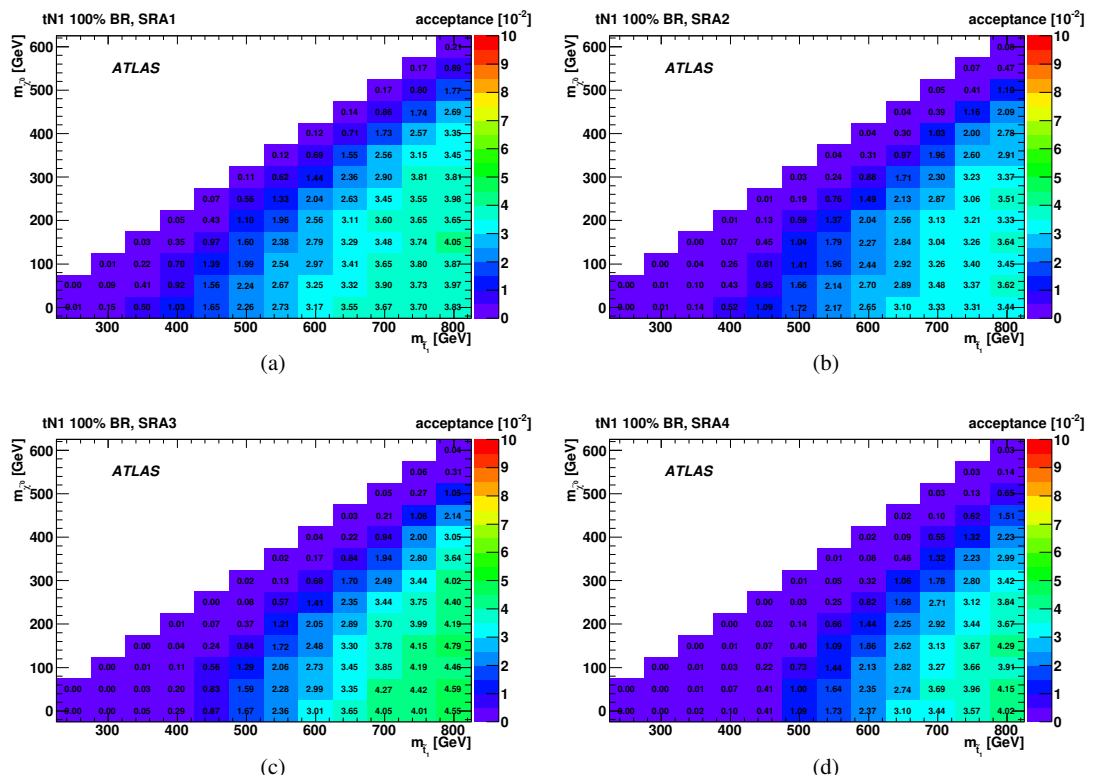
Reproduction of this article or parts of it is allowed as specified in the CC-BY-3.0 license.

Table 13: Cutflows for two representative signal models. The second column presents the cutflow for $\tilde{t}_1 \tilde{t}_1^*$ production where both top squarks decay via $\tilde{t}_1 \rightarrow t\tilde{\chi}_1^0$, for $m_{\tilde{t}_1} = 600$ GeV, $m_{\tilde{\chi}_1^0} = 1$ GeV (249, 999 generated events). The third column presents the cutflow for $\tilde{t}_1 \tilde{t}_1^*$ production for a signal sample where both top squarks decay via $\tilde{t}_1 \rightarrow b\tilde{\chi}_1^\pm$, for $m_{\tilde{t}_1} = 400$ GeV, $m_{\tilde{\chi}_1^\pm} = 100$ GeV, $m_{\tilde{\chi}_1^0} = 50$ GeV (40,000 generated events). For this latter sample, a generator-level filter is employed, requiring $E_T^{\text{miss}} > 60$ GeV and zero stable electrons or muons with $p_T > 10$ GeV within $|\eta| < 2.8$. The numbers in the table are normalized to $\int \mathcal{L} dt = 20.1 \text{ fb}^{-1}$.

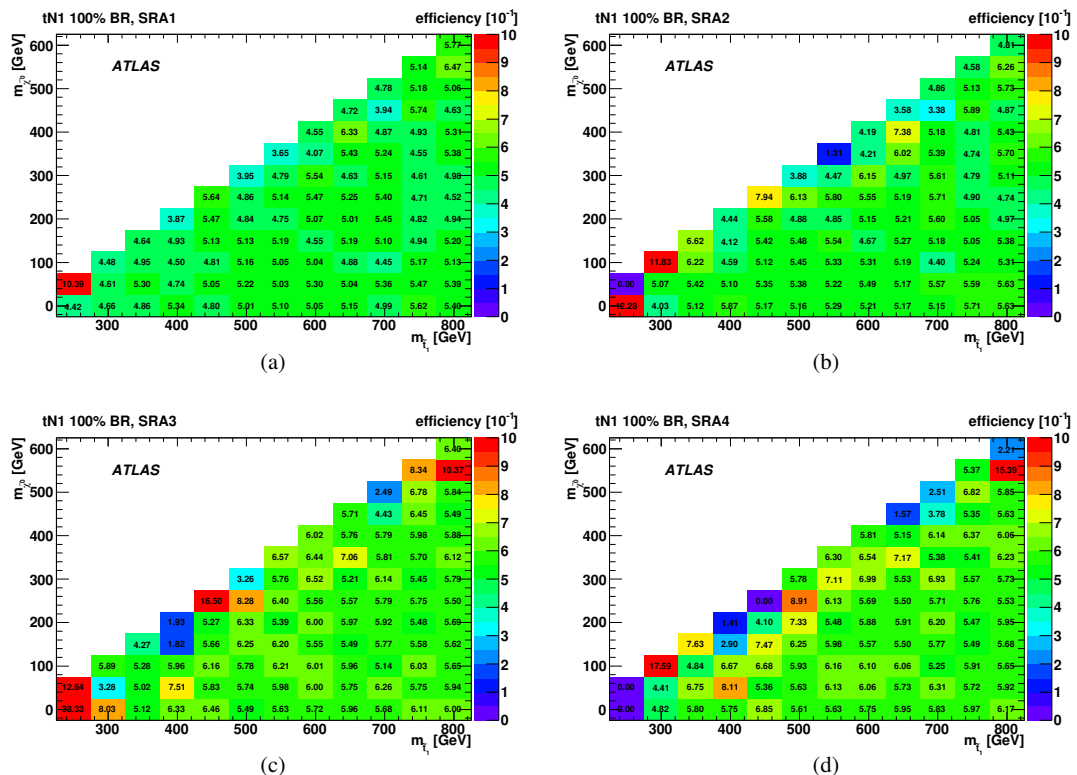
	Events in $\int \mathcal{L} dt = 20.1 \text{ fb}^{-1}$	
	$m_{\tilde{t}_1} = 600$ GeV, $m_{\tilde{\chi}_1^0} = 1$ GeV	$m_{\tilde{t}_1} = 400$ GeV, $m_{\tilde{\chi}_1^\pm} = 100$ GeV, $m_{\tilde{\chi}_1^0} = 50$ GeV
Trigger	460	1 856
Primary Vertex and Event Cleaning	451	1 831
Lepton Veto	285	1 777
$E_T^{\text{miss}} > 150$ GeV	252	1 009
SRA:		
≥ 6 jets	93	187
$ \Delta\phi(\text{jet}, \mathbf{p}_T^{\text{miss}}) > \pi/5, \Delta\phi(\mathbf{p}_T^{\text{miss}}, \mathbf{p}_T^{\text{miss,track}}) < \pi/3$	75	86
≥ 2 b -tagged jets	32	45
τ veto	28	32
$m_T^{b,\text{min}} > 175$ GeV	19	19
SRA1	8	2.1
SRA2	7	0.9
SRA3	9	0.6
SRA4	7	0.28
SRB:		
4 or 5 jets	97	248
$ \Delta\phi(\text{jet}, \mathbf{p}_T^{\text{miss}}) > \pi/5, \Delta\phi(\mathbf{p}_T^{\text{miss}}, \mathbf{p}_T^{\text{miss,track}}) < \pi/3$	94	207
≥ 2 b -tagged jets	29	97
$m_T^{b,\text{min}} > 175$ GeV	23	71
$m_{\text{jet}, R=1.2}^0 > 80$ GeV	20	33
$m_{\text{jet}, R=0.8}^0 > 50$ GeV	16	14
SRB1	2.6	0
SRB2	1.5	0.03
SRC:		
exactly 5 jets	62	210
$ \Delta\phi(\text{jet}, \mathbf{p}_T^{\text{miss}}) > \pi/5, \Delta\phi(\mathbf{p}_T^{\text{miss}}, \mathbf{p}_T^{\text{miss,track}}) < \pi/3$	52	90
≥ 2 b -tagged jets	18	43
τ veto	17	34
$ \Delta\phi(b, b) > 0.2\pi$	14	29
SRC1	9	17
SRC2	7	12
SRC3	6	6

Table 14: Summary of observed and expected CL_s values, using the best expected signal region combination, for each simulated $\tilde{t}_1 \rightarrow t\tilde{\chi}_1^0$ signal sample, where $B(\tilde{t}_1 \rightarrow t\tilde{\chi}_1^0) = 100\%$.

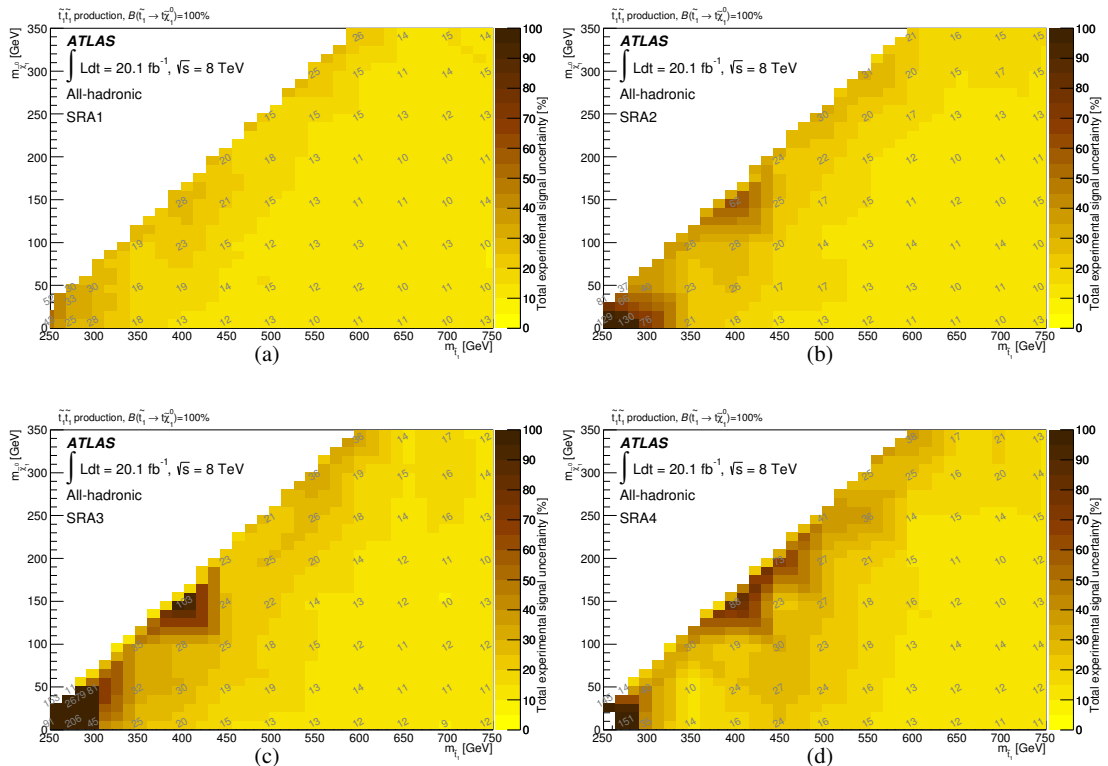
\tilde{t} mass [GeV]	$\tilde{\chi}_1^0$ mass [GeV]	Observed CL_s	Expected CL_s
250	1	5.272e - 02	4.685e - 01
250	25	6.512e - 02	4.622e - 01
250	50	5.000e - 01	8.860e - 01
275	1	7.710e - 04	2.432e - 02
275	25	4.705e - 03	9.675e - 02
275	50	2.271e - 02	3.241e - 01
275	75	6.980e - 02	6.509e - 01
300	1	1.300e - 05	6.760e - 04
300	50	6.450e - 04	1.798e - 02
300	100	1.125e - 01	8.046e - 01
350	1	1.000e - 06	1.000e - 06
350	50	1.000e - 06	3.000e - 06
350	100	4.300e - 05	2.858e - 03
350	150	7.238e - 02	7.103e - 01
400	1	1.000e - 06	1.000e - 06
400	50	1.000e - 06	1.700e - 05
400	100	4.300e - 05	1.930e - 03
400	150	1.373e - 03	3.652e - 02
400	200	8.386e - 02	7.602e - 01
450	1	1.000e - 06	3.000e - 06
450	50	1.000e - 06	1.200e - 05
450	100	2.000e - 06	2.030e - 04
450	150	6.800e - 05	3.879e - 03
450	200	4.795e - 03	1.105e - 01
450	250	8.746e - 02	7.775e - 01
500	1	3.000e - 06	8.000e - 06
500	100	4.700e - 05	1.330e - 04
500	150	8.690e - 04	2.231e - 03
500	200	2.869e - 03	7.642e - 02
500	250	1.928e - 02	3.166e - 01
500	300	9.919e - 02	8.609e - 01
500	320	1.291e - 01	9.396e - 01
500	50	1.100e - 05	3.300e - 05
550	1	1.770e - 04	1.630e - 04
550	50	1.130e - 04	1.060e - 04
550	100	4.220e - 04	4.020e - 04
550	150	2.097e - 03	1.955e - 03
550	200	1.259e - 02	3.155e - 02
550	250	6.166e - 02	1.362e - 01
550	300	4.720e - 02	5.552e - 01
550	350	1.214e - 01	9.266e - 01
600	1	1.438e - 03	1.558e - 03
600	50	1.318e - 03	1.417e - 03
600	100	3.264e - 03	3.471e - 03
600	150	9.778e - 03	1.099e - 02
600	200	2.076e - 02	2.328e - 02
600	250	4.779e - 02	1.134e - 01
600	300	1.255e - 01	2.761e - 01
600	350	7.809e - 02	7.510e - 01
650	1	2.328e - 02	1.213e - 02
650	50	1.605e - 02	2.057e - 02
650	100	1.204e - 02	1.496e - 02
650	150	2.742e - 02	3.410e - 02
650	200	3.986e - 02	4.934e - 02
650	250	1.031e - 01	1.316e - 01
650	300	2.115e - 01	2.885e - 01
650	350	2.248e - 01	4.838e - 01
700	1	6.576e - 02	4.807e - 02
700	50	7.517e - 02	4.741e - 02
700	100	1.345e - 01	1.038e - 01
700	150	1.284e - 01	9.479e - 02
700	200	1.298e - 01	9.445e - 02
700	250	1.356e - 01	1.773e - 01
700	300	3.130e - 01	2.649e - 01
700	350	3.169e - 01	4.358e - 01
750	1	2.341e - 01	2.059e - 01
750	50	2.181e - 01	1.868e - 01
750	100	2.509e - 01	2.160e - 01
750	150	2.609e - 01	2.325e - 01
750	200	2.620e - 01	2.443e - 01
750	250	3.501e - 01	3.138e - 01
750	300	4.058e - 01	3.795e - 01
750	350	3.034e - 01	4.600e - 01



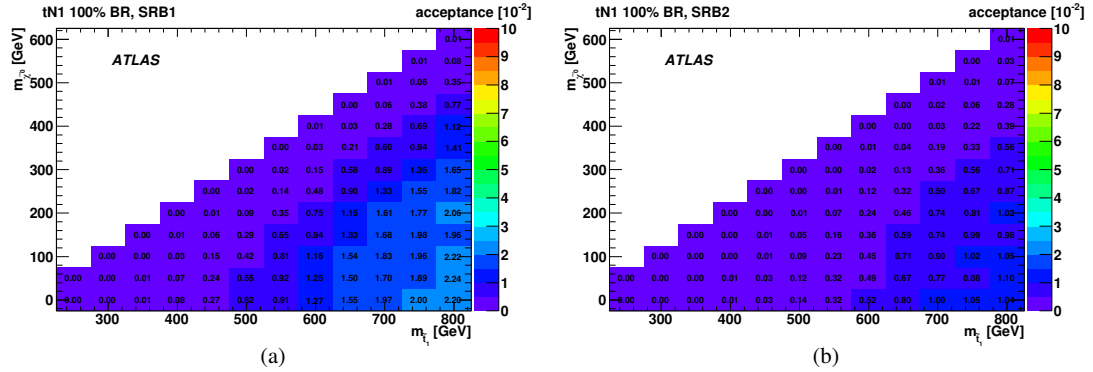
Aux. Fig. 10: Signal acceptances for SRA1 – 4 as a function of $m_{\tilde{t}}$ and $m_{\chi_1^0}$ for the $\tilde{t} \rightarrow \tilde{\chi}_1^0$ decay.



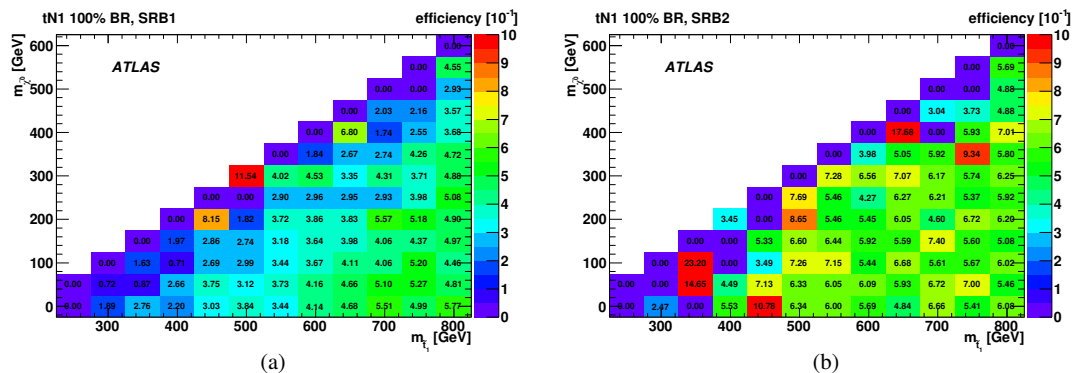
Aux. Fig. 11: Signal efficiency for selection of SRA1 – 4 as a function of $m_{\tilde{t}}$ and $m_{\tilde{\chi}_1^0}$ for the $\tilde{t} \rightarrow t \tilde{\chi}_1^0$ decay.



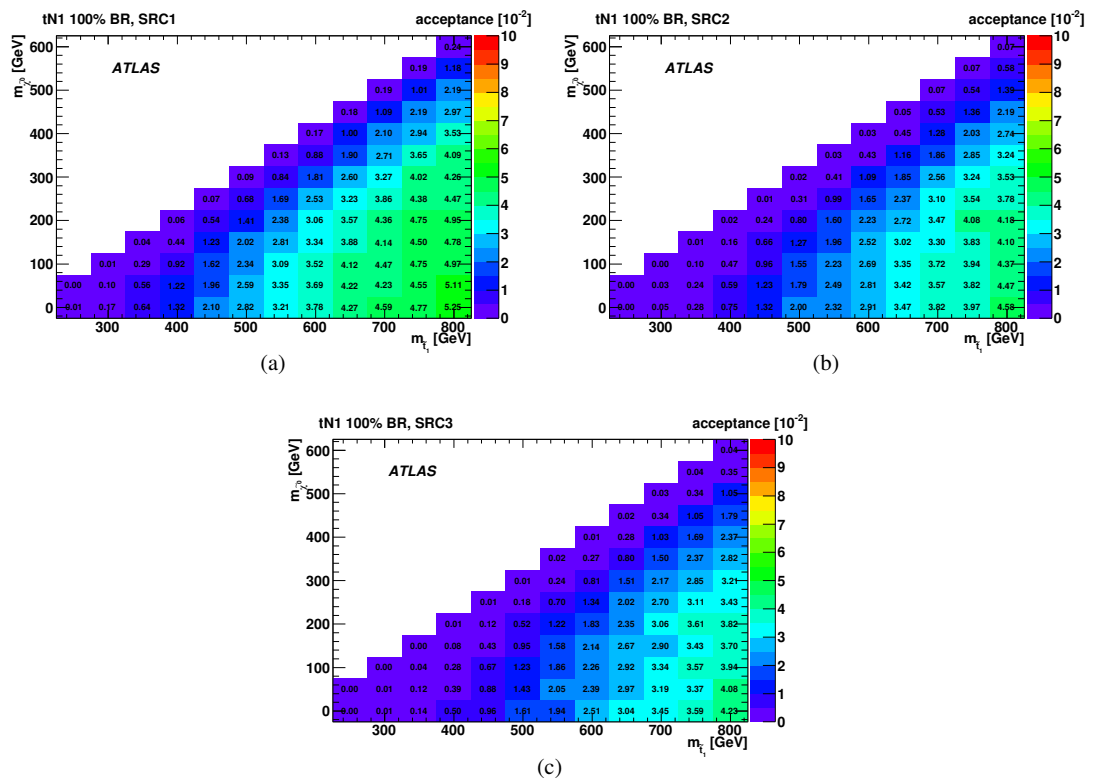
Aux. Fig. 12: Signal systematics for SRA1 – 4 as a function of $m_{\tilde{t}}$ and $m_{\tilde{\chi}_1^0}$ for the $\tilde{t} \rightarrow \tilde{t}\tilde{\chi}_1^0$ decay.



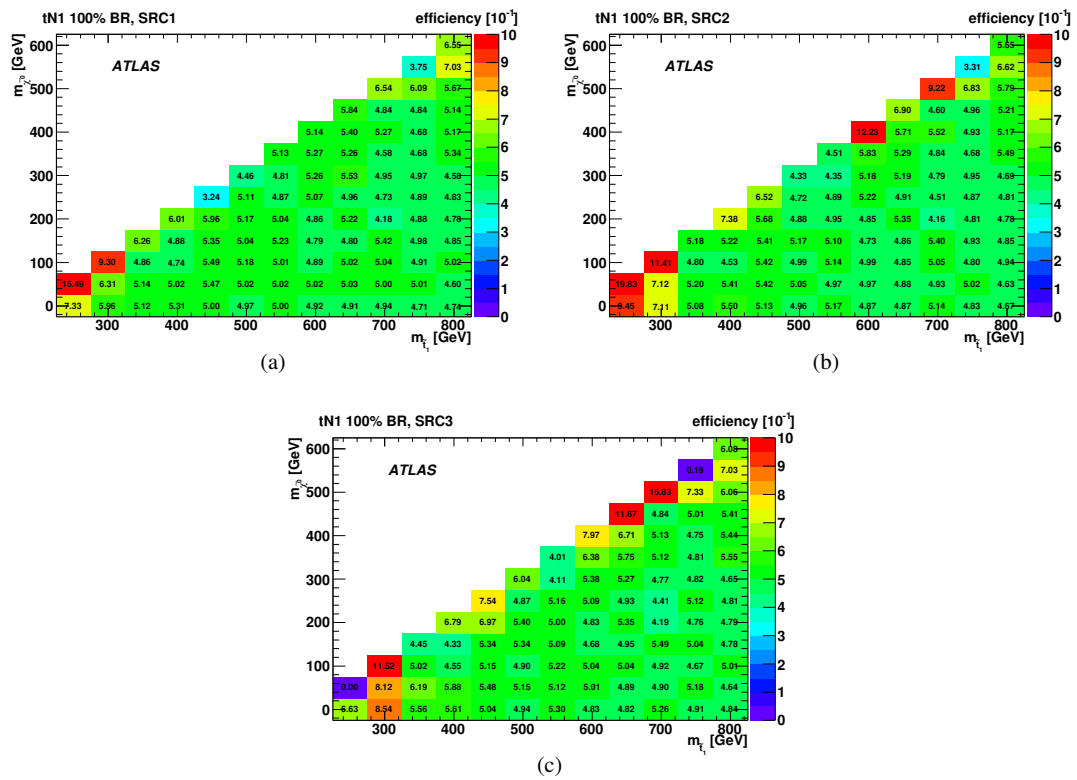
Aux. Fig. 13: Signal acceptances for SRB1 and SRB2 as a function of $m_{\tilde{t}}$ and $m_{\tilde{\chi}_1^0}$ for the $\tilde{t} \rightarrow t\tilde{\chi}_1^0$ decay.



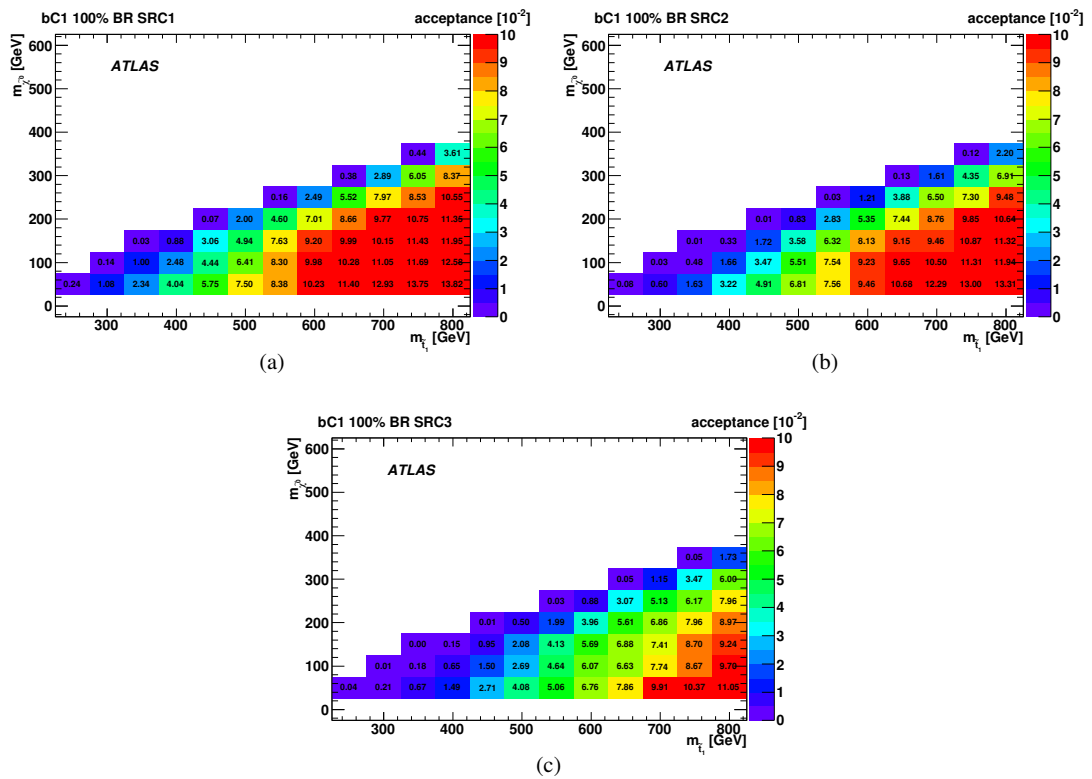
Aux. Fig. 14: Signal efficiency for the selection of SRB1 and SRB2 as a function of $m_{\tilde{t}}$ and $m_{\tilde{\chi}_1^0}$ for the $\tilde{t} \rightarrow t\tilde{\chi}_1^0$ decay.



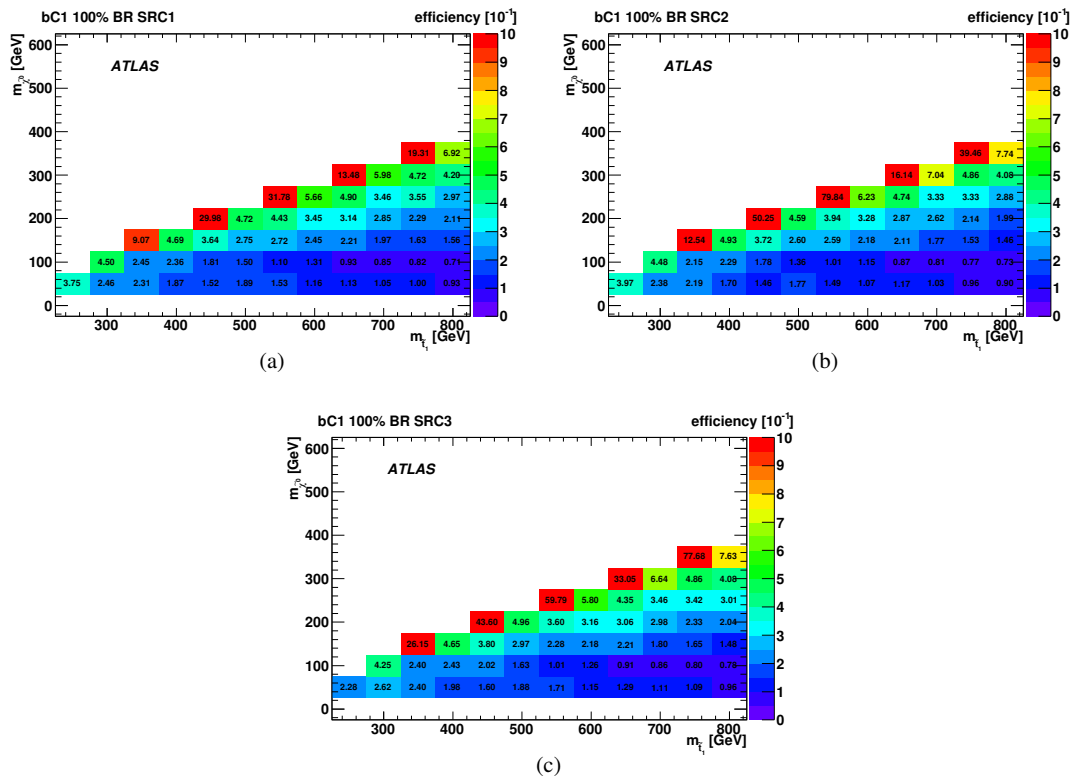
Aux. Fig. 15: Signal acceptances for SRC1 – 3 as a function of $m_{\tilde{t}}$ and $m_{\chi_1^0}$ for the $\tilde{t} \rightarrow t\tilde{\chi}_1^0$ decay.



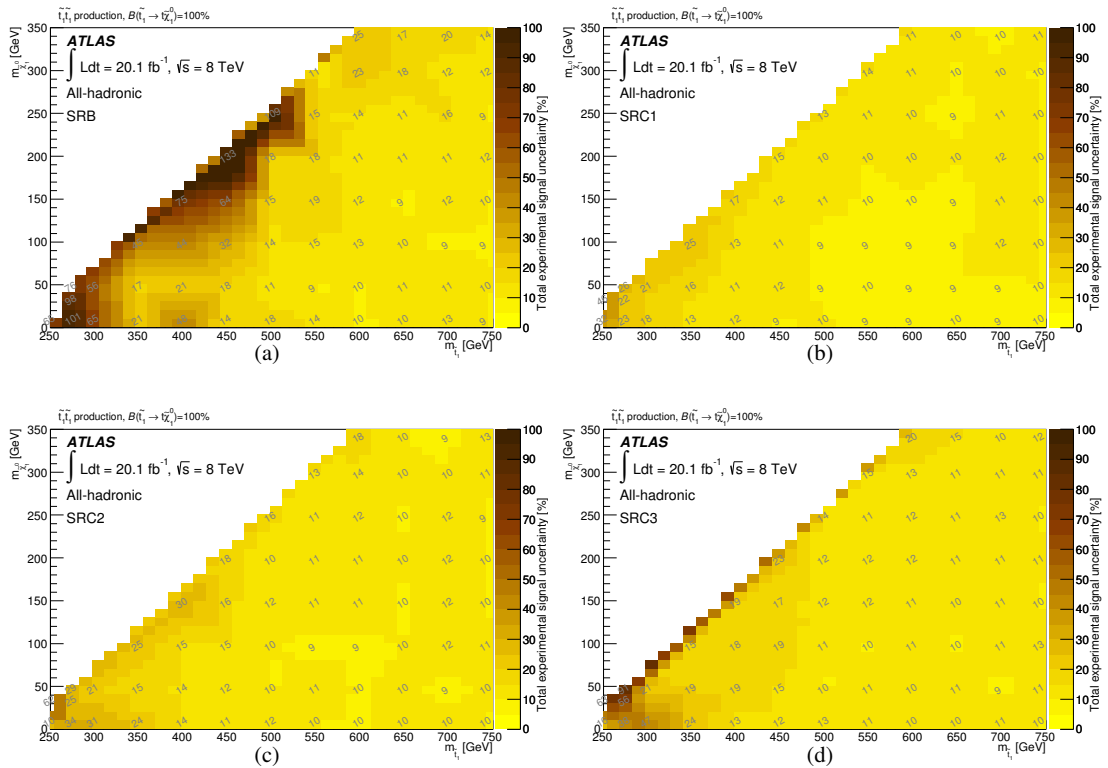
Aux. Fig. 16: Signal efficiency for the selection of SRC1 – 3 as a function of $m_{\tilde{t}}$ and $m_{\tilde{\chi}_1^0}$ for the $\tilde{t} \rightarrow t\tilde{\chi}_1^0$ decay.



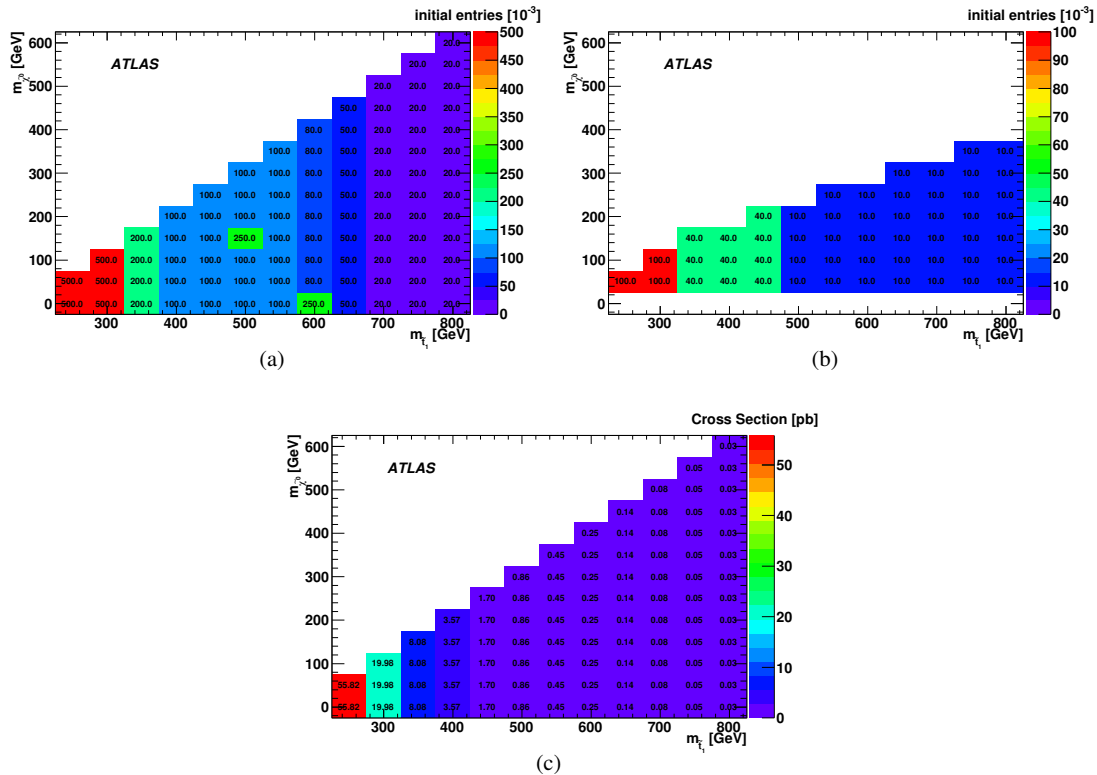
Aux. Fig. 17: Signal acceptances for SRC1 – 3 as a function of $m_{\tilde{t}}$ and $m_{\tilde{\chi}_1^0}$ for the $\tilde{t} \rightarrow b\tilde{\chi}_1^\pm$ decay.



Aux. Fig. 18: Signal efficiency for the selection of SRC1–3 as a function of $m_{\tilde{t}}$ and $m_{\tilde{\chi}_1^0}$ for the $\tilde{t} \rightarrow b\tilde{\chi}_1^\pm$ decay.



Aux. Fig. 19: Signal systematics for SRB (a) and SRC1 – 3, (b)–(d), as a function of $m_{\tilde{t}}$ and $m_{\tilde{\chi}_1^0}$ for the $\tilde{t} \rightarrow \tilde{\chi}_1^0$ decay.



Aux. Fig. 20: Number of generated events as a function of $m_{\tilde{t}}$ and $m_{\tilde{\chi}_1^0}$ for (a) the $\tilde{t} \rightarrow t\tilde{\chi}_1^0$ decay and (b) the $\tilde{t} \rightarrow b\tilde{\chi}_1^{\pm}$ decay. The \tilde{t} pair production cross section is shown in (c).